Nanoscale Horizons

ROYAL SOCIETY OF CHEMISTRY

REVIEW

View Article Online
View Journal | View Issue

Cite this: *Nanoscale Horiz.*, 2025, **10**, 2744

Multifunctional MEMS, NEMS, micro/nano-structures enabled by piezoelectric and ferroelectric effects

Mengyao Xiao, [ab] Aolei Xu,[ab] Zhouli Sui, [ab] Wenjie Zhang,[ab] Huajun Liu*[c] and Chengkuo Lee *[abde]

Received 31st May 2025,
Accepted 27th August 2025

DOI: 10.1039/d5nh00386e

rsc.li/nanoscale-horizons

MEMS and NEMS increasingly integrate multiple functions within compact platforms, enabled by piezoelectric and ferroelectric materials such as PZT, $BaTiO_3$, AlN, ScAlN, PVDF, and $Hf_{0.5}Zr_{0.5}O_2$. These materials support devices including mechanical sensors, RF resonators for gas detection, energy harvesters, non-volatile memories such as FeRAM and FeFETs, and neuromorphic computing arrays, as well as microspeakers and microphones for compact audio interfaces. They also play a key role in reconfigurable photonic components through acousto-optic and electro-optic modulation. This review examines materials, device designs, and integration strategies shaping next-generation intelligent microsystems across domains such as Artificial Intelligence of Things (AIoT), wearables, and robotics.

1. Introduction

Recently, advances in microelectromechanical systems (MEMS) and nanoelectromechanical systems (NEMS) have redefined the possibilities for integrated microscale functionality.[1–15] At the core of this transformation are piezoelectric[16–33] and ferroelectric[16,34–43] materials, which offer unique electromechanical coupling and tunable polarization behaviours. Piezoelectric materials convert mechanical deformation into electrical charge and *vice versa*, enabling their widespread use in sensors, actuators, resonators, and energy harvesters.[17,44] Ferroelectric materials, by contrast, exhibit spontaneous polarization that can be reversibly switched by an electric field, providing the physical basis for non-volatile memory, analog signal modulation, and neuromorphic computing.[42] Together, these material systems support multifunctional devices capable of sensing, actuating, storing, and processing information within a compact footprint.

To effectively design and integrate such devices across a broad range of MEMS and NEMS platforms, material selection becomes a critical consideration. The materials summarized in Table 1. Span a broad range of systems, each selected for its ability to meet the diverse requirements of MEMS and NEMS devices. Perovskite oxides such as PZT,[45–53] $BaTiO_3$,[52,54–57] and $PbTiO_3$[58–60] remain widely used because of their high piezoelectric coefficients and strong ferroelectricity, making them ideal for actuators, sensors, and non-volatile memories. In contrast, wurtzite semiconductors like AlN,[46,61–65] ScAlN,[62,66–71] GaN,[46,64,66,72] and ZnO[46,61,64,65,73] are valued for their low dielectric loss and excellent CMOS compatibility, which enables their integration into high-frequency resonators and filters. For applications requiring mechanical flexibility and low weight, ferroelectric polymers such as PVDF[50,54,74–80] allow the development of conformal devices for wearables and bio-integrated systems. Layered 2D materials (*e.g.*, MoS_2[81,82]) further push the limits of device miniaturization with atomically thin, tunable structures, while single crystals like $LiNbO_3$,[52,57,65,72,83,84] $LiTaO_3$,[61,66,83,85–87] and α-quartz[46,88] remain indispensable for acousto-optic and electro-optic modulation in photonic platforms. More recently, ferroelectric thin films such as $Hf_{0.5}Zr_{0.5}O_2$ (HZO)[89–92] have attracted attention for their scalability and CMOS process compatibility, offering a pathway toward embedded non-volatile memories and logic. Similarly, layered oxides (*e.g.*, $SrBi_2Ta_2O_9$ (SBT)[58,93,94]) and lead-free alternatives such as (K,Na)NbO_3 (KNN)[95–97] and $NaNbO_3$[98–100] are being explored to address environmental concerns. Each material class presents trade-offs among piezoelectric response, ferroelectric switching, mechanical robustness, and integration feasibility. Table 1 compares these materials across key parameters—including piezoelectric coefficients, remanent polarization, coercive field, and CMOS compatibility—to guide both device-level and system-level design.

Leveraging this material foundation, piezoelectric and ferroelectric MEMS/NEMS devices have been implemented across

[a] *Department of Electrical and Computer Engineering, National University of Singapore, Singapore 117576, Singapore. E-mail: elelc@nus.edu.sg*
[b] *Centre for Intelligent Sensors and MEMS (CISM), National University of Singapore, Singapore 117583, Singapore*
[c] *Institute of Materials Research and Engineering (IMRE), Agency for Science, Technology and Research (A*STAR), Singapore, Republic of Singapore. E-mail: liu_huajun@imre.a-star.edu.sg*
[d] *National University of Singapore Suzhou Research Institute (NUSRI), Suzhou Industrial Park, Suzhou 215123, China*
[e] *NUS Graduate School–Integrative Sciences and Engineering Programme (ISEP), National University of Singapore, Singapore 119077, Singapore*

Table 1 Summary of material properties and CMOS compatibility for piezoelectric and ferroelectric MEMS/NEMS devices

Materials	Piezoelectric stress coefficient	Piezoelectric strain coefficient (pm V^{-1})	Elastic modulus (Gpa)	Dielectric constant	Ferroelectric	Spontaneous polarization (μC cm^2)	CMOS compatibility	Ref.
PZT	$e_{31} \approx -5$ $e_{33} = 23.3$	$d_{31} = -171$ to 58 $d_{33} = 60–374$ $d_{15} = 584$	68	400–1400	✓	10–18	✗	45, 48–53 and 241–245
AlN	$e_{31} = -0.58$ $e_{33} = 1.55$ $e_{15} = -0.48$	$d_{31} = -2.0$ $d_{33} = 3.9$ $d_{22} = 21$	308	$\varepsilon_{r,11} = 8$ $\varepsilon_{r,33} = 9$	✗	—	✓	46 and 61–65
ScAlN	$e_{31} = -2.5$ (Sc 30%) $e_{33} = 2.3$ (Sc 30%)	$d_{31} = 7$ (Sc 30%) $d_{33} = 15–25$ (Sc 30%)	250 (Sc 30%) 269 (Sc 41%)	11.6 (Sc 10%) 13.7 (Sc 20%) 14 (Sc 30%)	✓ (Sc 27%)	80–155 (Sc 27%)	✓	62 and 66–71
ZnO	$e_{31} = -0.57$ $e_{33} = 1.32$	$d_{31} = -5.0$ $d_{33} = 5.9$	201	$\varepsilon_{r,11} = 7.41$ $\varepsilon_{r,33} = 7.82$	✗	—	✓	46, 61, 64, 65 and 73
$LiNbO_3$	$e_{31} = 0.23$ $e_{33} = 1.33$ $e_{22} = 2.43$ $e_{15} = 3.83$	$d_{31} = -1.0$ $d_{33} = 16$ $d_{22} = 20.8$ $d_{15} = 74$	203	$\varepsilon_{r,11} = 44.1$ $\varepsilon_{r,33} = 27.9$	✓	50	✗	52, 57, 65, 72, 83 and 84
$NaNbO_3$	—	$d_{33} = 1098–5024$	115–750	~30	✓	13.5	✗	98–100
$LiTaO_3$	$e_{31} = -0.11$ $e_{33} = 1.93$ $e_{22} = 1.67$ $e_{15} = 2.63$	$d_{31} = -3.0$ $d_{33} = 9.0$ $d_{22} = 7.5$ $d_{15} = 26$	233	$\varepsilon_{r,11} = 38.3$ $\varepsilon_{r,33} = 46.2$	✓	48–52	✗	61, 66, 83 and 85–87
$BaTiO_3$ (BTO)	$e_{31} = -0.7$ $e_{33} = 6.7$ $e_{15} = 34.2$	$d_{31} = -33.4$ $d_{33} = 90$ $d_{15} = 282–392$	222	$\varepsilon_{r,11} = 2200$ $\varepsilon_{r,11} = 56$	✓	26	✗	52 and 54–57
GaAs	$e_{31} = 0.093$ $e_{33} = 6.7$ $e_{15} = 34.2$	$d_{14} = 1.345$	118	12.9	✗	—	✗	61, 63, 64, 246 and 247
GaP	$e_{31} = 0.03$ $e_{33} = -0.07$ $e_{14} = -0.1$	$d_{14} = 1.9$	141	11.1	✗	—	✗	66, 248 and 249
GaN	$e_{31} = -0.33$ $e_{33} = 0.65$ $e_{15} = -0.33$ $e_{14} = 0.56$	$d_{33} = 3.1$	390	$\varepsilon_{r,11} = 9.5$ $\varepsilon_{r,11} = 10.6$	✗	—	✗	46, 64, 66 and 72
α-Quartz	$e_{11} = 0.17$ $e_{14} = 0.039$	$d_{31} = -0.09$ $d_{33} = 2.3$ $d_1 = 2.3$ $d_{14} = -0.67$	105.8	$\varepsilon_{r,11} = 4.5$ $\varepsilon_{r,11} = 4.63$	✗	—	—	46 and 88
PVDF	—	$d_{31} = 20–30$ $d_{33} = -40$ to 30	2.5–3	11	✓	6–14.5	✓	50, 54 and 74–80
PZT-5H	—	$d_{33} = -274$ $d_{33} = 593$ $d_{15} = 741$	—	—	✓	—	✗	52, 54 and 250
$Hf_{0.5}Zr_{0.5}O_2$(HZO)	—	$d_{33} = 1–17.8$	—	—	✓	12.2–16.2	✓	89–92
$PbTiO_3$ (PTO)	—	$d_{31} = -6.8$ $d_{33} = 56$ $d_{15} = 68$	988–1354	$\varepsilon_{r,11} = 240$ $\varepsilon_{r,11} = 190$	✓	57	✗	58–60
$BiFeO_3$ (BFO)	—	$d_{33} = 70$	—	—	✓	60–100	✗	58, 251 and 252
$SrBi_2Ta_2O_9$ (SBT)	—	$d_{33} = 13$	—	~200	✓	5–10	✓	58, 93 and 94
MoS_2	$e_{11} = 0.29$ C m^{-1}	—	—	—	✗	—	—	81 and 82
(K,Na)NbO_3 (KNN)	—	$d_{33} = 15–700$	—	177	✗	1.78–4.69	✓	95–97

multiple functional domains. These include mechanical sensors such as accelerometers,[101–106] pressure sensors,[101–103,105,107–113] and tactile arrays;[43,44,101,102,107,111,114–120] RF and acoustic resonators for signal processing and gas detection;[121–127] energy harvesters for battery-free operation;[128–137] and memory architectures such as FeRAM and FeFETs for embedded, non-volatile data storage.[35,36,39,138–145] In the audio domain, piezoelectric microspeakers[146–149] and microphones[150–152] offer compact and energy-efficient solutions for sound generation and capture. Additionally, ferroelectric materials enable emerging neuromorphic computing architectures through memristive arrays, while also playing a central role in acousto-optic modulators[48,61,66,153–177] and electro-optic waveguides,[178–185] where field-induced refractive index changes allow for dynamic frequency or phase control.

These functions are increasingly converging in real-world system-level applications. In AIoT (Artificial Intelligence of Things),[32,186–192] the integration of self-powered sensors,[22,29,188,189,193–201] local memory,[35,143,202–220] and computation[221–225] enables distributed edge nodes that operate autonomously. Wearable systems[226–229] benefit from flexible

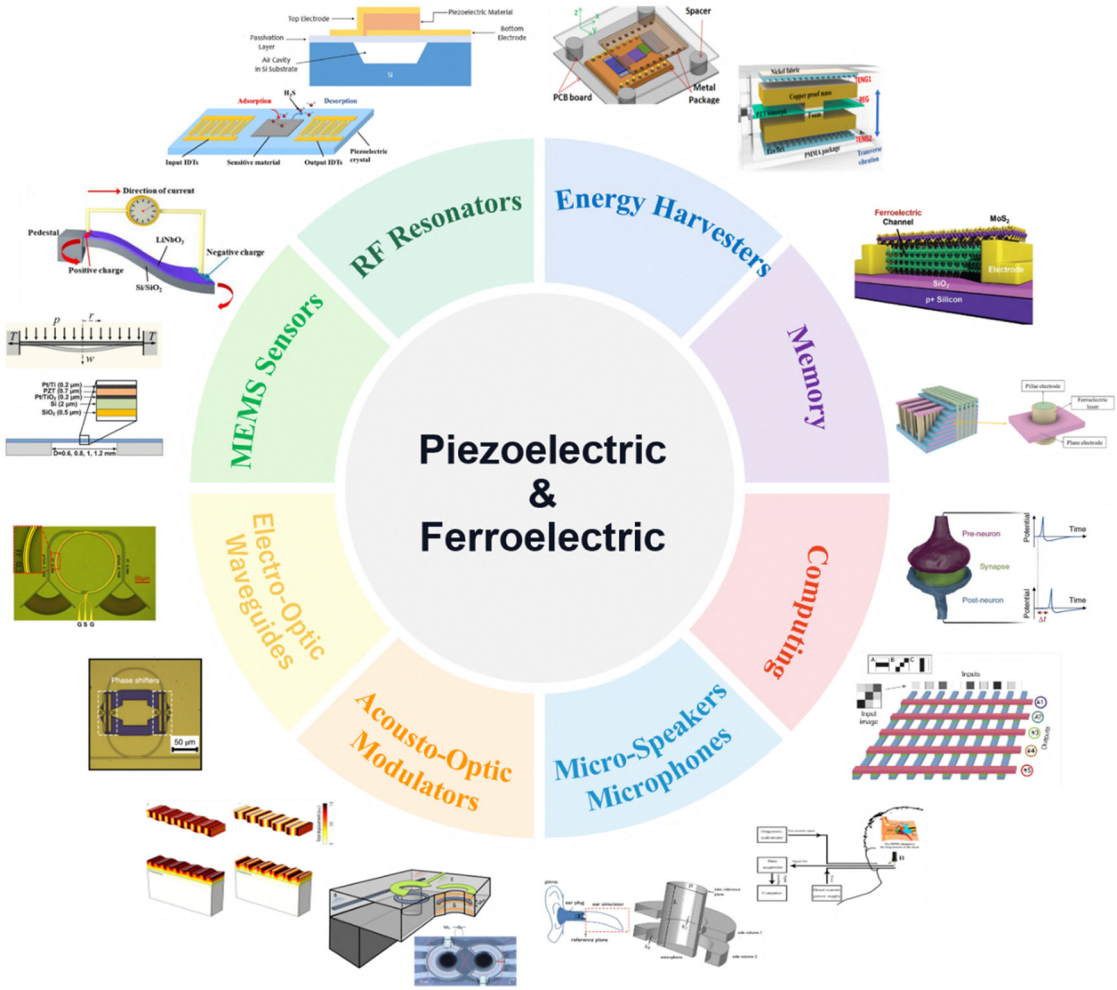

Fig. 1 Multifunctional MEMS/NEMS devices enabled by piezoelectric and ferroelectric effects across various domains.

piezoelectric tactile arrays for physiological monitoring and motion feedback, as well as audio interfaces enabled by micro-scale speakers and microphones. Electro-optic components based on ferroelectric thin films further support dynamic visual and data interfaces. In robotics, particularly soft and bio-inspired platforms,[189,230–240] piezoelectric tactile sensors and acoustic resonators facilitate high-resolution perception, while embedded ferroelectric logic units allow localized learning and control. As shown in Fig. 1, this convergence of sensing, memory, computation, and signal modulation into unified micro/nano-structures is not only feasible, but also actively shaping the foundation of next-generation smart systems.

2. MEMS sensors for mechanical stimuli detection

Thanks to rapid progress in piezoelectric materials and micro-fabrication technologies, a new class of MEMS sensors has emerged, offering high sensitivity and fast response in detecting mechanical stimuli. These sensors harness the piezoelectric effect to directly convert mechanical forces into electrical signals, eliminating the need for external power supplies. Their small size, low power consumption, and ease of integration make them well-suited for applications such as pressure sensing, strain detection, vibration monitoring, and inertial measurement. Depending on the nature of the signal they are designed to detect, these sensors can be broadly categorized into two groups: those that respond to static mechanical inputs and those tuned for dynamic stimuli. Fig. 2 presents a representative selection of MEMS sensors across this spectrum, each leveraging specific piezoelectric materials such as PZT,[104,111,113,253] AlN,[105,112] ZnO,[109] PVDF,[106] $LiNbO_3$,[103] and MoS_2.[254]

Among the different types of mechanical inputs that MEMS sensors respond to, static stimuli—such as steady pressure or strain—are often encountered in applications like tactile sensing[101] and biomedical diagnostics.[108] Several designs in Fig. 2 illustrate how piezoelectric materials are leveraged to achieve precise static sensing across a variety of configurations. For instance, Fig. 2(a) shows a circular diaphragm pressure sensor based on a multilayer PZT stack, where deflection under load generates a piezoelectric voltage signal.[113] This design

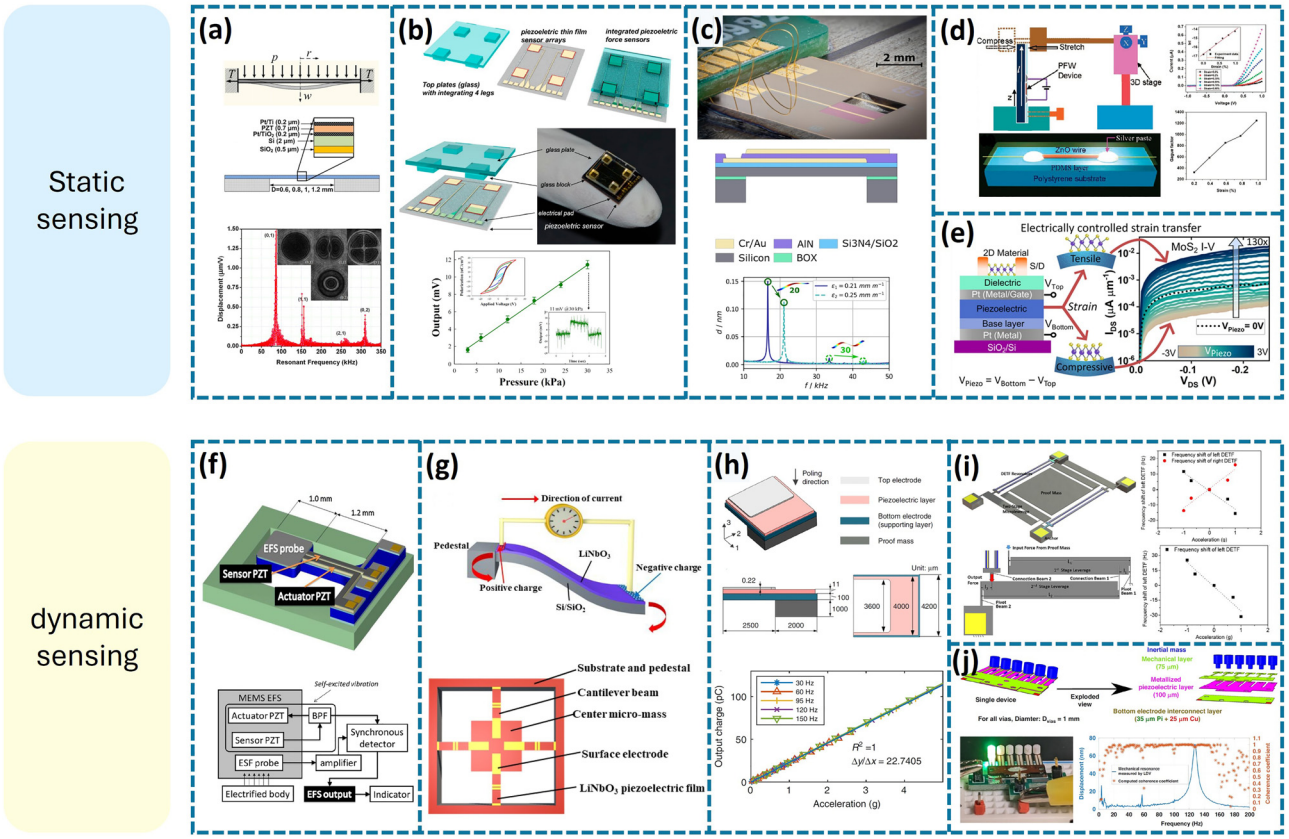

Fig. 2 Piezoelectric MEMS sensors for mechanical stimuli detection. (a) PZT diaphragm sensor for static pressure sensing. Reproduced with permission.[113] Copyright 2010, Elsevier B. V. (b) PZT thin-film array for static force detection *via* a suspended glass plate. Reproduced with permission.[111] Copyright 2014, by the authors; licensee MDPI, Basel, Switzerland. (c) AlN microbridge resonator for strain sensing through frequency shift. Reproduced with permission.[112] Copyright 2022, The Authors. Published by Elsevier B. V. (d) ZnO nanowire piezotronic strain sensor on flexible substrate. Reproduced with permission.[109] Copyright 2008, American Chemical Society. (e) MoS_2 FET with piezoelectric substrate for tunable static strain modulation. Reproduced with permission.[254] Copyright 2024, The Authors. Published by American Chemical Society. (f) Self-excited PZT cantilever for dynamic electrostatic field sensing. Reproduced with permission.[253] Copyright 2013, Elsevier B. V. (g) $LiNbO_3$ cantilever array for broadband vibration sensing. Reproduced with permission.[103] Copyright 2022, by the authors; licensee MDPI, Basel, Switzerland. (h) Thick-film PZT accelerometer with low noise and high sensitivity. Reproduced with permission.[104] Copyright 2023, The Author(s). Licensed under CC BY 4.0. Published by Springer Nature. (i) AlN-based in-plane resonant accelerometer with leverage-enhanced response. Reproduced with permission.[105] Copyright 2016, Elsevier B. V. (j) PVDF polymer accelerometer fabricated *via* laser micromachining and 3D printing. Reproduced with permission.[106] Copyright 2023, The Author(s). Licensed under CC BY 4.0. Published by Springer Nature.

achieves an average sensitivity of 280 Hz $mbar^{-1}$ in the 0–10 kPa range, which is 2.43 times higher than previously reported values (115 Hz $mbar^{-1}$), and a normalized sensitivity of approximately 3256 ppm $mbar^{-1}$, enabling precise pressure detection. This fundamental design remains widely used due to its simplicity and sensitivity. In a more complex structure, Fig. 2(b) integrates a PZT thin-film array beneath a suspended glass plate, supported by stress-concentrating legs.[111] This configuration provides a linear response across a pressure range of 3–30 kPa, delivering an output voltage from 1.8 mV at 3 kPa to 11 mV at 30 kPa, with good reproducibility across the four sensing units. This setup effectively localizes force input and enables linear static pressure detection, particularly valuable in medical force-feedback applications. Meanwhile, Fig. 2(c) moves into strain sensing territory, utilizing stress-engineered AlN thin films in a suspended microbridge resonator.[112] By tailoring intrinsic stress through deposition conditions, the device achieves a resonant frequency shift corresponding to a responsivity of approximately 17 000, nearly five times higher than conventional designs, while maintaining low residual stress (−170 MPa) and a piezoelectric coefficient of 5.76 pC N^{-1}. Flexible and nanoscale implementations also offer new directions for static sensing. In Fig. 2(d), a piezotronics strain sensor built from a ZnO nanowire responds to bending-induced stress by modulating its Schottky barrier height.[109] This device achieves a gauge factor as high as 1250, surpassing state-of-the-art CNT-based sensors (~1000) and conventional metal strain gauges (1–5), while offering excellent stability, reproducibility, and a fast response time of ~10 ms under repeated cyclic loading. And in Fig. 2(e), a MoS_2 field-effect transistor is strain-modulated through an underlying piezoelectric stack *via* the converse piezoelectric effect.[254] Electrical biasing enables reversible tuning between compressive (−0.23%) and tensile (+0.14%) strain, which modulates the drain current by 130×, on/off ratio by 150×, and mobility by 1.19×. The device

exhibits exceptionally high gauge factors of −1498 (compressive) and 1056 (tensile), highlighting its potential for programmable mechanical environments with precise and bidirectional strain control.

In contrast to static inputs, dynamic mechanical stimuli—such as vibrations, impacts, or transient accelerations—require sensors that respond to time-varying forces with speed and fidelity. Piezoelectric MEMS devices are inherently suited for such tasks due to their high-frequency responsiveness and strong electromechanical coupling. A representative example is the self-excited cantilever in Fig. 2(f), fabricated from PZT films, which operates as an electrostatic field sensor.[253] The cantilever vibrates continuously by amplifying and feeding back its piezoelectric output, enabling real-time detection of field-induced variations through shifts in oscillation behaviour. This device achieves reliable measurements over an electrostatic field range of −3 to +3 kV with good linearity at a resonant frequency of approximately 1875 Hz, while maintaining a stable self-excited vibration mode driven by an output voltage of about 0.12 Vpp. Dynamic acceleration sensing is showcased in Fig. 2(g), where a $LiNbO_3$-based cantilever array with a central proof mass transduces vibration into charge signals over a wide frequency range.[103] The sensor achieves a resonant frequency of 5.18 kHz and maintains stable output across 20 Hz–2.4 kHz with linear charge response to acceleration amplitudes from 5 g to 20 g. The sensitivity ranges from 6.1 to 10.3 pC g^{-1} along the *Z*-axis and 5.2 to 6.0 pC g^{-1} along the *X*/*Y* axes, with output charge amplitude reaching 61.4–102.8 pC at 10 g. Furthermore, the device remains functional from −40 °C to 70 °C, ensuring reliable performance in extreme environments. For low-noise and high-resolution applications, Fig. 2(h) introduces a cantilever accelerometer using aerosol-deposited thick PZT.[104] Leveraging well-aligned poling and optimized geometry, the device achieves a charge sensitivity of 22.74 pC g^{-1} with a natural frequency of 867.4 Hz and maintains a flat frequency response over 10–200 Hz (within ±5% error). The noise equivalent acceleration reaches as low as $5.6\,\mu g/\sqrt{Hz}$ at 20 Hz, enabling detection of accelerations above 279 μg (99.7% confidence), which makes it highly suitable for structural health monitoring and other precision vibration applications. Designs can also benefit from mechanical amplification, as seen in Fig. 2(i), an AlN-based in-plane resonant accelerometer that uses a two-stage leverage system to magnify inertial displacement.[105] Paired with centrosymmetric double-ended tuning fork (DETF) resonators, the device achieves a differential frequency sensitivity of 28.4 Hz g^{-1} at a base frequency of ∼140.7 kHz, corresponding to a relative sensitivity of 201 ppm g^{-1}, which is 57% higher than prior designs. This architecture combines compact size (2.0 × 1.6 mm^2) with high linearity ($R^2 \approx 0.946$), offering improved robustness against temperature drift through differential sensing. Finally, Fig. 2(j) demonstrates a novel direction in dynamic MEMS sensing with a fully polymeric accelerometer that employs 100 μm-thick PVDF films and 3D-printed support structures.[106] This design achieves a charge sensitivity of 21.82 pC g^{-1} (equivalent to 126.32 mV g^{-1} in open-circuit mode), a 5% flat bandwidth of 58.5 Hz, and a noise density of 6.02 $\mu g/\sqrt{Hz}$, enabling detection limits down to ∼258 μg (99% confidence). These metrics rival state-of-the-art PZT-based devices while offering simplified fabrication, miniaturization (90 mm^2 footprint), and a heavy-metal-free architecture for sustainable sensing applications.

Altogether, the examples in Fig. 2 underscore the remarkable versatility of piezoelectric MEMS sensors. By thoughtfully pairing materials such as PZT, AlN, ZnO, $LiNbO_3$, PVDF, and MoS_2 with carefully engineered microstructures, researchers have demonstrated a wide range of devices capable of detecting both static and dynamic mechanical signals with high sensitivity and robustness. As fabrication techniques continue to evolve and expand the material toolbox, we can expect MEMS sensors to play an increasingly central role in intelligent systems requiring real-time mechanical feedback—from wearable health monitors to autonomous robotics.

3. Application of piezoelectric RF resonators in gas sensing

The increasing demand for real-time, miniaturized, and highly sensitive gas detection technologies has driven significant interest in acoustic wave-based sensors, particularly radio frequency (RF) resonators such as film bulk acoustic resonators (FBARs) and surface acoustic wave (SAW) devices.[255] These resonators operate on the principle of mass loading, where the adsorption of gas molecules onto a functional sensing layer results in measurable shifts in the resonant frequency, as shown in Fig. 4(b).[256] Compared with traditional analytical techniques like gas chromatography–mass spectrometry (GC-MS), which are often bulky and unsuitable for field use, RF resonators offer the advantages of compactness, low power consumption, and fast response, making them ideal candidates for portable and integrated gas sensing platforms.[255] To illustrate the progress in this field, Table 2 summarizes representative SAW- and FBAR-based gas sensors, highlighting their functional materials, detection limits, and response dynamics. However, while most studies focus on achieving high sensitivity, limited attention has been given to the challenge of cross-sensitivity—*i.e.*, the sensor's response to non-target gases or environmental variations such as humidity and temperature. This limitation highlights the need for future work on strategies such as selective coatings, sensor arrays, or advanced compensation algorithms to improve gas selectivity and enhance robustness for practical deployment.

3.1. SAW resonators for surface-sensitive detection

Among RF-based devices, surface acoustic wave (SAW) devices are widely used for gas sensing due to their sensitivity to surface perturbations. When gas molecules adsorb onto a sensing film, they alter the wave propagation characteristics—typically velocity or amplitude—leading to measurable signal changes. These devices are typically built on piezoelectric substrates such as quartz (ST-cut), lithium ehavio ($LiNbO_3$), or lithium ehavior ($LiTaO_3$), which support stable and efficient acoustic wave generation. The choice of substrate and wave mode, including Rayleigh or shear-horizontal (SH) waves, plays

Table 2 Performance comparison of SAW- and FBAR-based gas sensors using different functional materials

Device Type	Substrate	Sensing layer	Target gases	Detection limit	Sensitivity	Frequency	Response/recovery	Ref.
SAW	$LiNbO_3/SiO_2/SiC$	GQDs-PEI-SiO_2	Humidity	–	2.4 MHz/%RH	5.9 GHz	20 s/5 s	125
SAW	128° *YX*-$LiNbO_3$	$Cu_3(HHTP)_2$ MOF	H_2S (NH_3, CO_2 tested)	6 ppb	0.02 mV ppb^{-1}	200 MHz	281 s/—	126
SAW	$LiNbO_3$	MFU-4/MFU-4l (MOF)	CO_2 (N_2, H_2O vapor tested)	~1 ppm	Phase shift-based detection	56.2–293 MHz	3.5 s/1.3 s	121
SAW	$LiNbO_3$	rGO-PPy/Ag (UV-activated)	NO_2 (CO_2, CO, HCHO, H_2, NH_3 tested)	2.37 ppm	127.68 Hz ppm^{-1}	~247 MHz	36.7 s/58.5 s	124
SAW	ST-cut Quartz	SnO_2 quantum wires	NO_2 (H_2S, NH_3, SO_2, H_2, ethanol tested)	21 ppb	1.69 ppm^{-1}	~199.5 MHz	55 s/96 s	122
FBAR	Si + AlN	PEI-modified SWNTs	Formaldehyde (acetone, ethanol, methanol tested)	24 ppb	1.472 kHz ppb^{-1}	~4.5 GHz	47.3 s/58.6 s	257
FBAR	AlN	MOF (HKUST-1) + PDMS + SAM	Water, methanol, ethanol, *n*-propanol, alkanes	1.51–6.85 ppm	0.28–1.27 × 10^3 Hz ppm^{-1}	2.4 GHz	~70 s/reversible	258
FBAR	Si + AlN	PCL/PIB polymers (array)	Acetone, *n*-pentane, *n*-hexane, *n*-heptane	~1 ppm	Up to 20× enhancement	1.21 GHz	Reversible, few seconds	259
FBAR	Si + AlN	PSS/PDDA (Layer-by-layer)	Methanol, ethanol, acetone, IPA, toluene, cyclohexane	40 ppm	0.13 (MeOH) to 0.002 (C_6H_{12}) kHz ppm^{-1}	~2.45 GHz	3–8 s (heating)/ 10–18 s (cooling)	260

a critical role in determining the device's sensitivity, frequency range, and environmental robustness. As shown in Fig. 3(a), a typical SAW sensor includes interdigital transducers (IDTs) on a piezoelectric substrate, with a functional film deposited along the acoustic path to enable selective detection.[1]

To improve sensitivity and enable higher frequency operation, ultrahigh frequency shear-horizontal SAW (SH-SAW) devices have been developed using thin-film $LiNbO_3$ on a SiC substrate.[125] As shown in Fig. 3(b), the device consists of a 220 nm $LiNbO_3$ film (34° *Y–X* cut) atop a SiO_2 buffer layer and SiC support, with Al electrodes forming the interdigital transducers. The sensing layer is a ternary nanocomposite composed of polyethyleneimine (PEI), silica nanoparticles (SiO_2 NPs), and graphene quantum dots (GQDs), enabling efficient humidity adsorption. This SH-SAW structure operates at 4.7 GHz and 5.9 GHz, offering rapid response and high sensitivity due to both the high operating frequency and the strong interaction between water molecules and the functional film. Recent work has also been explored by integrating advanced porous materials like conductive metal–organic frameworks (MOFs). To enable ppb-level detection of toxic gases, surface acoustic wave (SAW) sensors functionalized with conductive metal–organic frameworks (MOFs) have shown significant promise.[126] As illustrated in Fig. 3(c), a SAW device was integrated with $Cu_3(HHTP)_2$ MOFs as the sensing layer, deposited along the acoustic path between interdigital transducers on a 128° *YX*-cut lithium ehavio ($LiNbO_3$) substrate. This MOF provides open metal sites for selective H_2S adsorption, enhancing both mass loading and acoustoelectric effects. Operating at 200 MHz, the sensor achieved a theoretical detection limit of ~6 ppb and demonstrated high sensitivity (0.02 mV ppb^{-1}) at room temperature, with excellent selectivity over common interfering gases. These results highlight the potential of combining high-performance piezoelectric substrates with engineered conductive MOFs for ultra-low concentration gas detection. Beyond enhancing sensitivity, SAW devices also enable kinetic analysis of gas interactions. To study gas uptake kinetics, SAW sensors coated with microporous MOFs have been employed.[121] As shown in Fig. 3(d), a delay-line SAW device on *Y*-cut $LiNbO_3$ was coated with MFU-4 and MFU-4l crystals, which differ in pore aperture. The sensor uses three IDTs to monitor phase shifts during CO_2 exposure. MFU-4l, with larger pores, showed faster and stronger responses than MFU-4, demonstrating the sensor's ability to distinguish diffusion behavior based on molecular size. Material engineering further supports low-temperature operation. To improve room-temperature NO_2 sensing, a SAW device was developed using a 3D porous rGO–Ppy/Ag aerogel as the sensing layer.[124] As shown in Fig. 3(e), the sensor is built on a *Y*-cut 128° lithium nionate ($LiNbO_3$) substrate with interdigital transducers (IDTs) patterned in a delay-line configuration. The hybrid aerogel combines reduced graphene oxide (rGO), polypyrrole (PPy), and silver nanoparticles to provide a high surface area and active adsorption sites. UV activation further enhances the response by generating photocarriers that accelerate NO_2 adsorption and desorption. The sensor demonstrates fast response/recovery times (36.7 s/58.5 s),

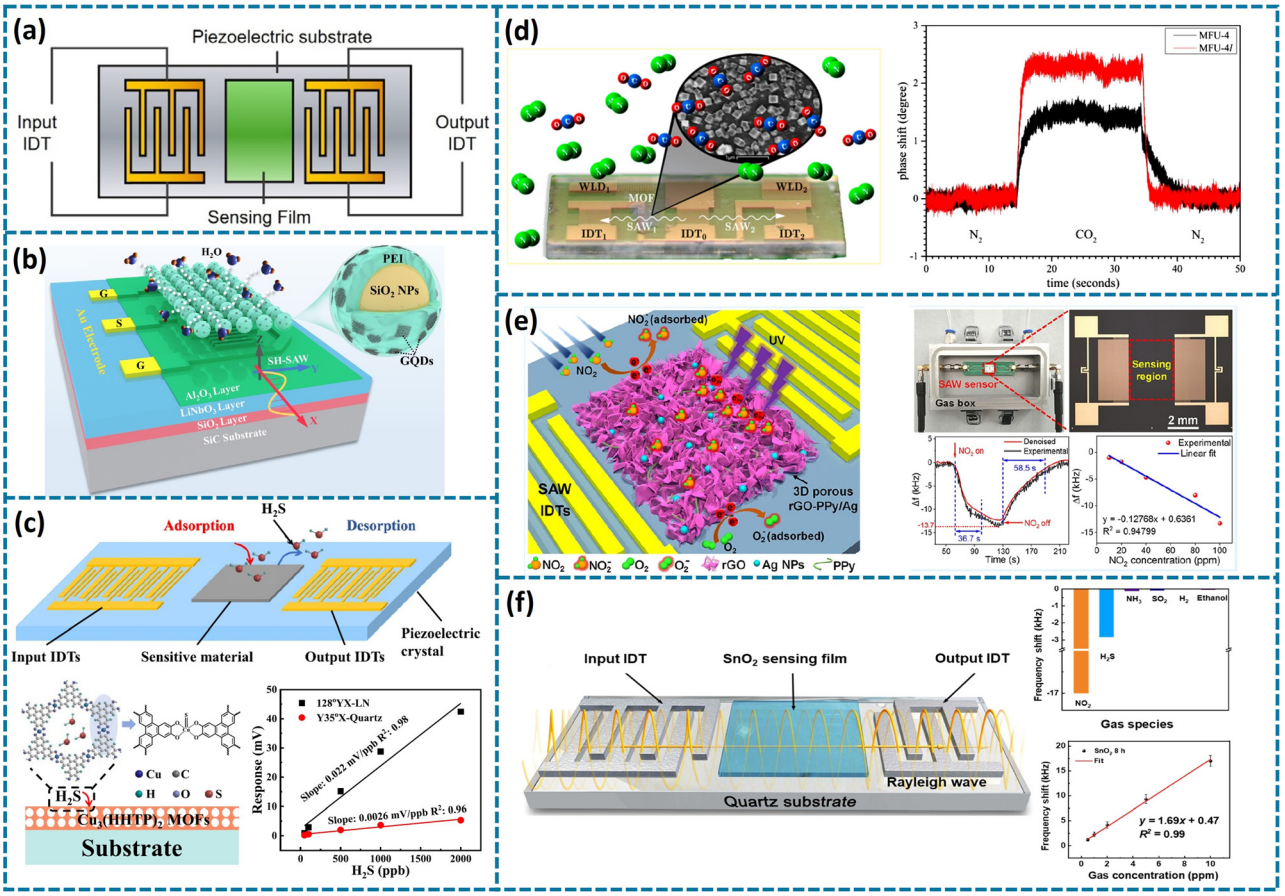

Fig. 3 Surface acoustic wave (SAW) gas sensors and material strategies. (a) Schematic of a typical SAW device with interdigital transducers (IDTs) and a functional sensing layer. Reproduced with permission.[1] Copyright 2024, The Author(s). Small science published by Wiley-VCH GmbH. (b) SH-SAW device using thin-film $LiNbO_3$ on SiC with a ternary nanocomposite layer for humidity sensing. Reproduced with permission.[125] Copyright 2023, Elsevier B. V. (c) $Cu_3(HHTP)_2$ MOF-coated SAW sensor for ppb-level H_2S detection. Reproduced with permission.[126] Copyright 2024, Elsevier B. V. (d) Delay-line SAW sensor with MFU-4/MFU-4l coatings for monitoring CO_2 uptake kinetics. Reproduced with permission.[121] Copyright 2017, American Chemical Societ€(e) UV-activated SAW sensor using a 3D rGO–PPy/Ag aerogel for NO_2 detection. Reproduced with permission.[124] Copyright 2021, American Chemical Society. (f) SAW sensor on ST-cut quartz with facet-engineered SnO_2 quantum wires for selective NO_2 sensing. Reproduced with permission.[122] Copyright 2022, Elsevier B. V.

high sensitivity (127.68 Hz ppm^{-1}), and good linearity, making it suitable for real-time environmental monitoring. Complementary to material hybridization, crystal facet engineering also improves performance. To achieve selective and sensitive NO_2 detection, a SAW sensor was developed using facet-engineered SnO_2 quantum wires as the sensing film.[122] As shown in Fig. 3(f), the device is constructed on an ST-cut quartz substrate, which offers excellent temperature stability. The interdigital transducers (IDTs) generate Rayleigh waves across a SnO_2-coated acoustic path. By optimizing the synthesis time to increase the exposure of (110) facets, the SnO_2 film enhances NO_2 adsorption and mass loading. The sensor demonstrates a linear response over 0.5–10 ppm, a detection limit of 21 ppb, and excellent selectivity against interfering gases such as NH_3 and SO_2.

3.2. FBAR resonators for high-frequency sensing

In parallel, film bulk acoustic resonators (FBARs) offer another compact and highly sensitive platform enabled by the piezoelectric effect. A typical structure of a film bulk acoustic resonator (FBAR) is shown in Fig. 4(a). FBARs are built on a silicon substrate where an air cavity is etched beneath the resonator to confine the acoustic wave in the thick direction of the piezoelectric layer. The device consists of a piezoelectric thin film—commonly Lead Zirconate Titanate ($Pb(Zr_xTi_{1-x})O_3$), aluminum nitride (AlN) or zinc oxide (ZnO)[261,262]—sandwiched between a top and bottom electrode. When an alternating electric field is applied, longitudinal acoustic waves are generated and reflected between the two electrodes. The air cavity acts as an acoustic reflector, enabling the resonance condition by minimizing energy leakage into the substrate. The passivation layer provides environmental protection and electrical insulation. Resonance occurs when the thickness of the piezoelectric film corresponds to half the wavelength ($\lambda/2$) of the applied RF signal. This design enables operation in the GHz frequency range, offering higher sensitivity compared to surface acoustic wave (SAW) sensors. Due to this, FBARs are particularly advantageous for high-resolution, miniaturized, and CMOS-compatible gas sensing platforms.[255]

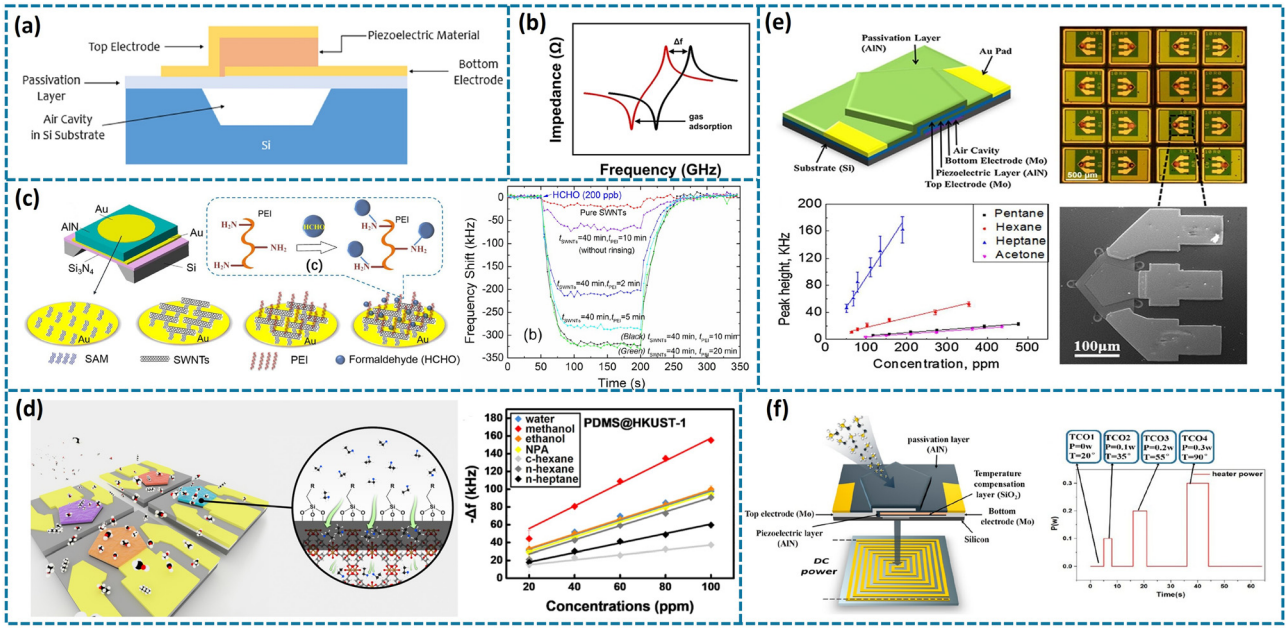

Fig. 4 Film bulk acoustic resonator (FBAR) gas sensors and advanced designs. (a) Cross-sectional schematic of a typical FBAR structure with air cavity and piezoelectric layer. Reproduced with permission.[255] Copyright 2022, Elsevier B. V. (b) Working principle of mass loading-induced frequency shift in acoustic resonators. Reproduced with permission.[256] Copyright 2022, The Author(s). Licensed under CC BY 4.0. Published by AIP Publishing. (c) AlN-based FBAR with PEI-modified SWNT layer for formaldehyde sensing. Reproduced with permission.[257] Copyright 2018, Elsevier B. V. (d) FBAR array functionalized with HKUST-1 MOF and PDMS coating for multi-VOC detection. Reproduced with permission.[258] Copyright 2020, American Chemical Soc€y. (e) Miniaturized FBAR sensor array integrated with GC column for VOC analysis. Reproduced with permission.[259] Copyright 2018, Elsevier B. V. (f) Temperature-modulated FBAR with microheater enabling virtual sensehaviorbehaviour. Reproduced with permission.[260] Copyright 2019, American Chemical Society.

As shown in Fig. 4(c), the FBAR sensor functionalized with polyethyleneimine (PEI)-modified single-walled carbon nanotubes (SWNTs) exhibited a strong response to formaldehyde gas at a concentration of 200 ppb.[257] The device was constructed using a piezoelectric stack of Au (100 nm)/AlN (1 μm)/Au (100 nm), where aluminum nitride (AlN) served as the piezoelectric layer due to its high acoustic velocity, excellent chemical stability, and compatibility with CMOS fabrication processes. The optimized device—with a SWNT assembly time of 40 minutes and PEI modification time of 10 minutes—achieved a maximum frequency shift of approximately 325 kHz, significantly outperforming sensors with only PEI or SWNT layers. The enhanced sensitivity is attributed to the large surface area provided by the SWNT network and the selective binding of formaldehyde molecules by the amine groups in PEI, which form reversible Schiff base linkages. This combination of material engineering and high-frequency acoustic transduction illustrates the potential of AlN-based FBARs for trace-level VOC sensing. Fig. 4(d) shows the sensing performance of a film bulk acoustic resonator (FBAR) array functionalized with HKUST-1 metal–organic framework (MOF) and coated with a thin PDMS layer.[258] This array format supports real-time, multi-analyte detection in compact devices. Each FBAR consists of a 1 μm thick aluminum nitride (AlN) piezoelectric film sandwiched between molybdenum electrodes, operating at ~2.4 GHz. This array configuration enables high-throughput, real-time detection of various volatile organic compounds (VOCs) at concentrations from 20 to 100 ppm. The sensors exhibit distinct frequency shifts for different analytes, with methanol and water showing the strongest responses due to strong interactions with hydrophilic sites in HKUST-1. The PDMS layer further enhances selectivity and environmental stability, making the array suitable for integrated multi-gas detection platforms. Additionally, self-assembled monolayer (SAM)-coated FBAR arrays have demonstrated concentration-independent VOC responses, enabling selective detection without thermal modulation.[263] This approach supports simplified multi-gas sensing and electronic nose applications. Fig. 4(e) shows a miniaturized FBAR sensor array integrated with a GC system for vapor detection.[259] Each FBAR consists of a 1 μm thick aluminum nitride (AlN) piezoelectric layer sandwiched between molybdenum electrodes, built on a silicon substrate with an air cavity for acoustic isolation. A top AlN passivation layer provides protection. The array includes multiple polymer-coated sensors, enabling selective detection of VOCs such as pentane, hexane, heptane, and acetone. Operating at 1.21 GHz, the sensors exhibit linear frequency shifts with increasing concentration, with acetone showing the strongest response due to its interaction with carbonyl-sensitive coatings. This array-based design supports quantitative analysis of complex gas mixtures with high sensitivity and low power consumption. Fig. 4(f) illustrates a temperature-modulated film bulk acoustic resonator (FBAR) sensor integrated with a programmable micro-heater to enable virtual sensor array (VSA) operation.[260]

The FBAR consists of a molybdenum (Mo) top and bottom electrode sandwiching a 0.39 μm thick aluminum nitride (AlN) piezoelectric layer, with an additional 0.07 μm SiO_2 temperature compensation layer to suppress thermal drift. A 0.19 μm AlN passivation layer is deposited on top for chemical and mechanical protection. By dynamically varying heater power from 0 W to 0.3 W, the device is modulated across temperatures from 20 °C to 90 °C. This enables the same FBAR sensor to mimic a multiparameter sensor array by generating distinct responses to volatile organic compounds (VOCs) under different thermal conditions. The resulting frequency shifts serve as multidimensional features for vapor discrimination using PCA or LDA, allowing for over 97% classification accuracy among six VOCs.

In addition to conventional FBARs, the solidly mounted resonator (SMR) structure has emerged as a robust alternative. By using Bragg reflectors instead of air cavities, SMRs improve mechanical stability and simplify surface processing. For example, oxygen plasma-treated GO-coated SMRs have shown enhanced NH_3 sensitivity due to increased surface defect density and better nanomaterial integration.[264] More recently, multi-degree-of-freedom (Multi-DoF) BAW resonators on AlN-on-SOI platforms have enabled dual-mode sensing.[265] With ZIF-8 coatings, both frequency and amplitude ratio responses were used to detect ethanol vapor, showing improved sensitivity and higher *Q*-factors than traditional designs.

Overall, these developments highlight the central role of the piezoelectric effect in enabling acoustic wave-based gas sensing. By converting electrical signals into mechanical vibrations and *vice versa*, piezoelectric materials such as AlN, ZnO, $LiNbO_3$, and PZT form the foundation of both SAW and FBAR devices. Advances in piezoelectric film engineering, device architecture, and functional surface coatings have significantly enhanced the sensitivity, selectivity, and integration potential of these resonators. As a result, the application of piezoelectricity in RF resonators continues to drive progress toward compact, real-time, and highly responsive gas sensors suitable for diverse and demanding environments.

4. MEMS energy harvesters for self-powered microsystems

Piezoelectric MEMS energy harvesters have emerged as key enablers for self-powered microsystems, particularly in applications such as structural health monitoring, wearable electronics, and wireless sensor networks. These harvesters convert ambient mechanical energy—such as vibration, footstep, or structural strain—into electrical energy based on the piezoelectric effect, wherein mechanical stress induces electric polarization in non-centrosymmetric materials.[137] Typically, the direct piezoelectric effect is employed in energy harvesting, generating voltage from applied stress, while the converse effect enables actuation by applying electric fields.[128] In recent studies, a range of piezoelectric materials and structural designs have been developed. For example, PZT thin films are commonly used in MEMS cantilever-based systems for broadband vibration harvesting;[131] PVDF and ceramic composites are embedded in wearable platforms like shoes and floors due to their mechanical flexibility;[134] and hybridized structures integrating TENG with piezoelectric energy generator (PEG) enable multi-modal harvesting and sensing.[130] These innovations demonstrate the adaptability of piezoelectric technology to diverse scenarios, balancing energy output, device footprint, and structural resilience.

A MEMS piezoelectric energy harvester is developed using a dual-cantilever structure with mechanical stoppers to enable a broadened operational bandwidth. The system, shown in Fig. 5(a), consists of a high-frequency cantilever (PEH-T) and a low-frequency cantilever (PEH-B) arranged face-to-face, where the proof mass of PEH-B can impact both the upper and lower stoppers during vibration. Lead zirconate titanate (PZT) thin film is used as the piezoelectric layer on both cantilevers to convert mechanical strain into electrical energy. These impact-induced interactions introduce nonlinear stiffness and trigger frequency up-conversion (FUC), effectively extending the working bandwidth. The device achieves a frequency range of 30–48 Hz and generates 34–100 nW under 0.6 g acceleration, making it suitable for variable-frequency energy harvesting.[132] A hybridized energy harvesting system integrating both piezoelectric and triboelectric mechanisms has been developed for autonomous wireless sensing in harsh environments. The system employs a lead zirconate titanate (PZT) bimorph as the piezoelectric energy generator (PEG) and two contact-separation mode TENGs as self-powered acceleration sensors and stoppers. The PEG is excited through impact with the TENG stoppers, achieving broadband output performance. This multifunctional configuration, illustrated in Fig. 5(b), enables simultaneous vibration energy harvesting and acceleration monitoring. The harvested energy powers a low-consumption Arduino-based wireless node, while the TENG provides acceleration sensing. Demonstration tests in a train-like environment show that the system can wirelessly transmit acceleration data *via* Zigbee, supporting real-time monitoring without external power.[129] A scrape-through MEMS energy harvester is developed to realize frequency broadening and up-conversion by coupling two cantilevers with distinct resonant frequencies. In this design, a low-frequency cantilever (PZT-L) with an attached proof mass interacts periodically with a high-frequency cantilever (PZT-H) and a metal base during vibration. Lead zirconate titanate (PZT) is employed as the piezoelectric material on both cantilevers to convert dynamic strain into electrical energy. When the excitation amplitude is sufficiently high, the PZT-L cantilever impacts and scrapes through the PZT-H cantilever, triggering frequency up-conversion and enhancing energy harvesting performance. The device achieves an extended bandwidth of 33–43 Hz and generates up to 94 nW output under a 0.6 g base acceleration. As shown in Fig. 5(c), experimental results confirm that the hybrid motion of the two beams significantly improves power output in low-frequency, broadband environments.[135] In Fig. 5(d), a smart floor tile integrates cantilever-based piezoelectric harvesters to capture mechanical energy from human steps. Each 20 × 20 cm^2 tile contains a harvester unit that, when compressed, generates

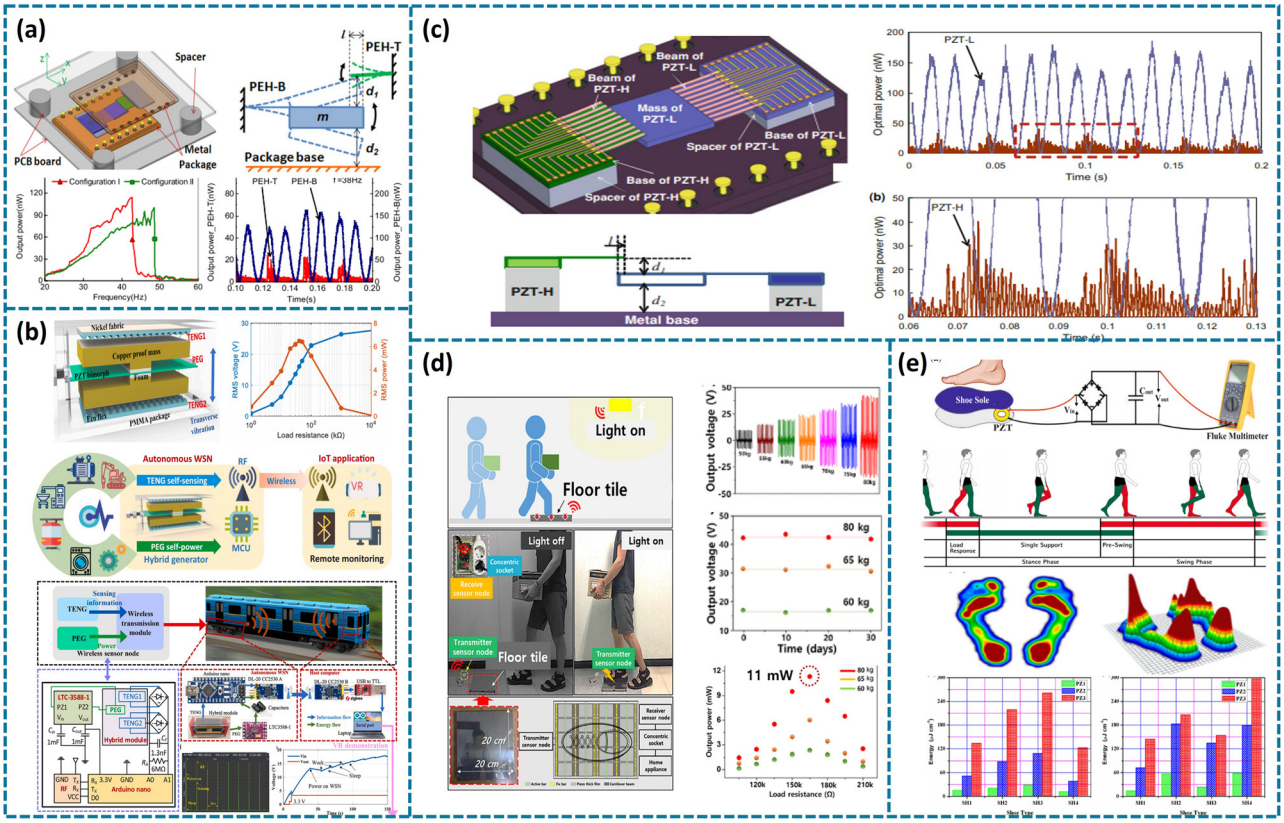

Fig. 5 MEMS energy harvesters for self-powered microsystems. (a) Schematic illustration of a dual-cantilever MEMS energy harvester with mechanical stoppers for bandwidth enhancement and frequency up-conversion. Reproduced with permission.[132] Copyright 2012, IOP Publishing. (b) Schematic of a hybrid TENG–PEG energy harvester integrated in a train environment for wireless sensing and power generation. Reproduced with permission.[129] Copyright 2021, Elsevier. (c) Schematic of a scrape-through MEMS harvester utilizing a low-frequency cantilever impacting a high-frequency cantilever to induce self-oscillation. Reproduced with permission.[135] Copyright 2011, Springer Nature. (d) Schematic of a piezoelectric floor tile-based system for real-time control of smart home appliances using harvested human motion energy. Reproduced with permission.[133] Copyright 2018, Elsevier. (e) Schematic of a shoe-embedded piezoelectric energy harvester with plantar mapping analysis and gait-based energy generation. Reproduced with permission.[136] Copyright 2020, Spring Nature.

enough energy to drive a wireless transmitter. The device uses a PZN-0.5C composite ceramic, formulated as $0.72Pb(Zr_{0.47}Ti_{0.53})O_3$–$0.28Pb[(Zn_{0.45}Ni_{0.55})_{1/3}Nb_{2/3}]O_3$ + CuO, as the piezoelectric material, offering high transduction efficiency and stable output under repeated loading. This enables remote switching of home appliances such as lighting and HVAC systems. Long-term tests demonstrate stable performance across varying user weights and durations, making it a robust solution for self-powered control in intelligent home and building systems.[133] A wearable energy harvesting approach embeds a piezoelectric PZT buzzer into the insole of a shoe, where footstep pressure induces electrical output *via* the d_{33} effect. The buzzer is composed of lead zirconate titanate (PZT) ceramic, offering high piezoelectric coefficient and mechanical robustness. As depicted in Fig. 5(e), the energy generated from heel strike and toe-off motions is rectified and stored for later use. Pressure mapping experiments using force plates and plantar sensors reveal that the harvester performs best in block- or wedge-heeled shoes and when placed near the toe region. The design offers a low-cost, unobtrusive method for generating power in wearable systems.[136]

To provide a clearer comparison of different MEMS energy harvester designs, Table 3 summarizes the key performance metrics (*e.g.*, power density, bandwidth, and output voltage/power) of representative designs shown in Fig. 5(a–e).

Although recent progress has brought MEMS energy harvesters closer to real-world deployment, several integration challenges remain. These include: (1) packaging requirements to protect against mechanical stress and humidity; (2) size limitations imposed by microsystem footprints; and (3) electrical compatibility with existing CMOS circuits and energy storage modules. Overcoming these constraints will be key to realizing robust, miniaturized, and system-level integrated harvesters for IoT and biomedical applications.

Collectively, the energy harvesting systems represent a progression from MEMS-based resonant cantilevers to large-area and wearable implementations. The diversity of piezoelectric materials, including PZT films, PZT bimorphs, and PZN-0.5C ceramics, as well as structural configurations such as dual cantilevers, bimorph beams, scrape-through mechanisms, and embedded designs, showcases the engineering flexibility of piezoelectric harvesters. These approaches not only enhance

Table 3 Comparison of key performance metrics for MEMS piezoelectric energy harvesters

Working principle/device type	Material	Power density ($\mu W\ cm^{-3}$)	Bandwidth (Hz)	Output voltage (V)	Output power(μW)	Ref.
Piezoelectric (MEMS cantilever)	PZT	12.9	267–350	3.4 V (peak)	5.15	131
Hybridized TENG & PEG	PZT, PDMS	230	3–1 k	45 V (TENG) + 12 V (PEG)	120	128
Piezoelectric (scrape-through beam)	PZT	10.4	600–700	3.0 V (peak)	2.48	134
Piezoelectric (U-shaped beam)	PZN-0.5C composite ceramic	20.2	70–90	8.4 V (peak)	7.6	132
Piezoelectric (shoe embedded)	PZT ceramic	2.5	1–3	Max 1.5 V (AC)	4.2	135

energy conversion efficiency across variable-frequency and impacted environments but also offer practical integration into smart infrastructure and mobile platforms. In particular, the inclusion of a performance comparison table and discussion of integration challenges further strengthens th' section's practical value and facilitates engineering adoption.

5. Ferroelectric-based memory and computing devices

Ferroelectric materials not only enable reliable non-volatile memory[37,141] through reversible polarization switching but also underpin emerging memristive devices that emulate synaptic plasticity for neuromorphic computing.[36,141,266] Building on this versatility, ferroelectric thin films are first integrated into FeRAM and FeFET architectures to achieve high-speed, low-power data storage. More recently, these films have been adapted into memristor arrays that combine storage and processing within the same physical substrate, enabling in-memory computation and accelerating brain-inspired learning.

5.1. Ferroelectric non-volatile memories

Ferroelectric non-volatile memories (FeNVMs) represent a class of memory technologies that leverage the bistable polarization states of ferroelectric materials to store digital information without continuous power supply.[141,267] Two primary device implementations include ferroelectric random-access memory (FeRAM), which uses a capacitor-based 1T–1C structure, and ferroelectric field-effect transistors (FeFETs), which embed a ferroelectric layer into the gate stack of a MOSFET to enable non-destructive readout and enhanced scalability.[42] These devices have attracted widespread interest due to their fast-switching speed, low operating voltage, and compatibility with CMOS processes, making them promising candidates for embedded non-volatile memory and logic-in-memory applications. As illustrated in Fig. 6(a), FeRAM (left) features a discrete ferroelectric capacitor paired with a transistor, while FeFET (right) integrates the ferroelectric thin film directly within the gate dielectric, enabling higher integration density and more efficient memory access.[42] Common ferroelectric materials used in these devices include perovskite-type oxides such as AlScN[268] and emerging HfO_2-based materials like $Hf_{0.5}Zr_{0.5}O_2$[38,214,269] and Al-doped HfO_2,[39] which offer CMOS compatibility and scalability.[37,42]

Fig. 6(b–d) focus on material and structural strategies for FeRAM devices. In Fig. 6(b), phase engineering of $Hf_{1-x}Zr_xO_2$-based ferroelectric capacitors is presented to achieve hysteresis-free, pseudo-linear dielectric behaviour.[270] This is critical for improving the reliability and integration of MFM-based FeRAM. Si doping helps suppress polarization switching by stabilizing the amorphous phase, while La doping enhances the anti-ferroelectric phase, increasing the dielectric constant without causing hysteresis. These approaches enable better control of the polarization response and improve FeRAM scalability. Fig. 6(c) illustrates a three-dimensional (3D) vertically stacked ferroelectric capacitor structure, designed for FeRAM applications. The device uses a TiN/Al-doped HfO_2/TiN stack and incorporates a pillar electrode architecture to increase the active area without enlarging the footprint. This structure enables multiple ferroelectric capacitors to share a common vertical electrode, improving integration density and reducing power consumption. The cross-sectional TEM image confirms the layered structure and uniformity, while the polarization–voltage (P–V) curves show strong ferroelectric switching with a remanent polarization (2Pr) over 20 $\mu C\ cm^{-2}$ and low coercive voltage ($\sim$2.7 V). These characteristics, along with high endurance ($>10^6$ cycles) and long retention (10 years), demonstrate the potential of this 3D capacitor design for scalable and reliable FeRAM memory cells.[39] A ferroelectric tunnel junction (FTJ) is employed to build a plasmon-electron addressable FeRAM device, as shown in Fig. 6(d).[214] The structure consists of a thin HfO_2 ferroelectric layer ($\sim$5 nm) sandwiched between two Au electrodes. The device writes memory states using surface plasmon polaritons (SPPs) and reads them *via* tunneling current. Polarization switching in the HfO_2 layer modulates the tunneling barrier, leading to a bistable I–V response that enables non-volatile memory storage. This hybrid design, combining optical writing and electrical reading, is compatible with CMOS processes and offers promise for low-power, high-speed FeRAM applications. Recent studies on $Hf_{0.5}Zr_{0.5}O_2$ thin-film capacitors have reported ultrahigh dielectric permittivity by stabilizing the non-centrosymmetric orthorhombic phase.[269] These improvements enhance polarization strength and scalability, supporting high-density and low-voltage FeRAM applications.

In addition to conventional FeRAMs, recent studies have introduced alternative ferroelectric memory architectures that

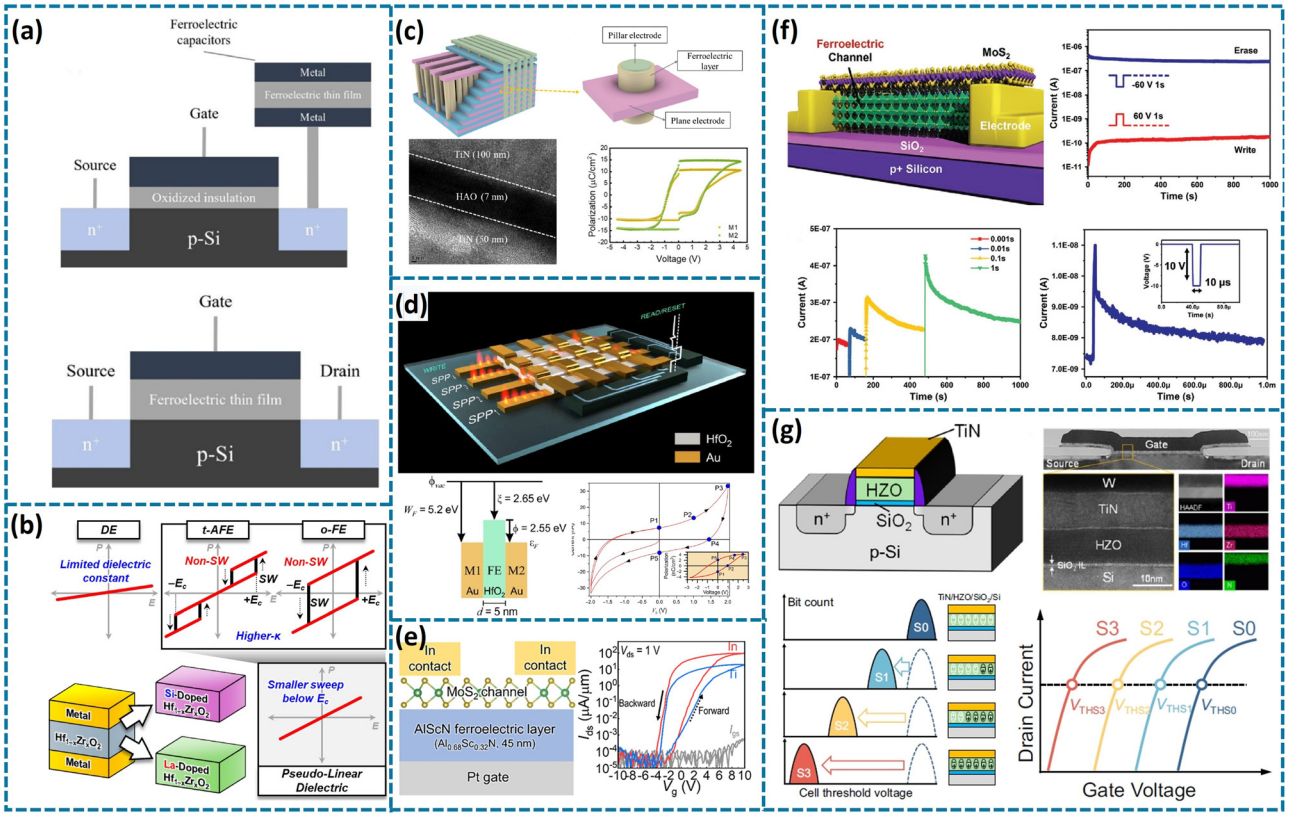

Fig. 6 Ferroelectric non-volatile nemories (FeNVMs). (a) Comparison between FeRAM and FeFET architectures: FeRAM uses a separate ferroelectric capacitor in a 1T–1C configuration, while FeFET integrates a ferroelectric layer into the gate dielectric of a MOSFET, enabling non-destructive readout and higher integration density. Reproduced with permission.[271] Copyright 2024, Elsevier B. V. (b) Phase engineering of $Hf_{1-x}Zr_xO_2$ to tune dielectric behaviour and suppress hysteresis through Si and La doping. Reproduced with permission.[270] Copyright 2025, The Author(s). Licensed under CC BY 4.0. Published by Springer Nature. (c) Three-dimensional stacked ferroelectric capacitor based on Al-doped HfO_2 for improved integration and remanent polarization. Reproduced with permission.[39] Copyright 2025, American Chemical Society. (d) Ferroelectric tunnel junction (FTJ) using an ultrathin HfO_2 layer for plasmon-assisted optical writing and tunneling-based electrical reading. Reproduced with permission.[214] Copyright 2025, The Author(s). Licensed under CC BY 4.0. Published by AAAS. (e) A monolayer MoS_2 FeFET with an AlScN ferroelectric gate dielectric showing strong ferroelectric switching and high on/off ratio. Reproduced with permission.[41] Copyright 2025, American Chemical Society. (f) MoS_2/2D perovskite ferroelectric channel transistor (FcFET) demonstrating multilevel switching and fast programming. Reproduced with permission.[40] Copyright 2024, Wiley-VCH GmbH (g) Multibit FeFET-based CAM array using threshold-controlled states for low-power edge AI applications. Reproduced with permission.[38] Copyright 2025, The Author(s). Licensed under CC BY 4.0. Published by Springer Nature.

utilize polarization-modulated resistive switching, commonly referred to as ferroelectric resistive random-access memory (FeRRAM) or ferroelectric memristors. One such example involves a composition-graded ScAlN-based metal–ferroelectric–semiconductor (MFS) structure, which enables highly controllable multilevel storage through engineered polarization gradients.[35] This structure achieves up to 7-bit resolution, linear weight updates, and low-voltage operation, making it well-suited for neuromorphic computing and analog in-memory processing. Another notable approach employs a [001]-oriented $NaNbO_3$ film in a metal–insulator–metal (MIM) configuration to realize a self-rectifying, self-powered resistive switching device.[212] This device exploits ferroelectric polarization to modulate the Schottky barrier at the metal/ferroelectric interface, enabling selector-free, energy-autonomous operation. These advances expand the design space of FeNVMs beyond FeFET and FeRAM architectures, highlighting the versatility of ferroelectric materials in enabling multifunctional, low-power memory systems for next-generation intelligent electronics.

Fig. 6(e–g) focus on ferroelectric field-effect transistors (FeFETs), which integrate a ferroelectric layer into the gate stack of a MOSFET structure. As shown in Fig. 6(e), a ferroelectric field-effect transistor (FeFET) is constructed using a monolayer MoS_2 channel and a 45 nm-thick $Al_{0.68}Sc_{0.32}N$ (AlScN) ferroelectric gate dielectric.[268] The use of AlScN provides a high remanent polarization ($Pr \approx 80$–$115\ \mu C\ cm^{-2}$), enabling strong electrostatic modulation of the channel. The In-contact electrodes minimize contact resistance and allow efficient carrier injection, resulting in high on-current ($\sim 120\ \mu A/\mu m$ at $V_{ds} = 1$ V) and a large I_{on}/I_{off} ratio ($\sim 2 \times 10^7$). The device shows clear counter-clockwise hysteresis in the transfer characteristics, confirming the ferroelectric switching behaviour. This design demonstrates excellent potential for high-performance and scalable non-volatile memory applications based on 2D FeFETs. Fig. 6(f) highlights a ferroelectric channel field-effect transistor (FcFET)

based on a MoS_2/2D perovskite heterojunction.[40] In this architecture, the 2D Ruddlesden–Popper perovskite serves directly as the channel material, enabling both semiconducting and ferroelectric properties within a single layer. This differs from conventional FeFETs that use ferroelectrics solely as gate dielectrics. The device exhibits a remarkably wide memory window of up to 177 V, a high on/off ratio of $\sim 5 \times 10^5$, and strong nonvolatile behaviour with retention over 1000 s and endurance beyond 10^3 cycles. Benefiting from charge trapping and polarization switching, the FcFET also demonstrates multilevel conductance control and sub-10 μs programming, underscoring its potential for future neuromorphic and high-density memory systems. Fig. 6(g) illustrates a multilevel FeFET array for in-memory computing, demonstrating both memory and logic capabilities.[38] The FeFET device features a TiN/HZO/SiO_2/Si gate stack, as confirmed by cross-sectional TEM imaging. By applying different program pulses, the transistor exhibits four distinct threshold voltage states (S0 to S3), enabling multibit data storage in a single cell. This characteristic is used to implement a content-addressable memory (CAM) array for low-power edge detection tasks. The threshold voltages correspond to specific conductance levels, and matching operations are performed by sensing current responses across different gate voltages. This multilevel operation allows for both exact and fuzzy feature matching, making it well suited for edge AI tasks that require fast, energy-efficient decision making. The system achieves sub-10 fJ per operation energy consumption and supports non-volatile, analog-to-digital converter (ADC)-free readout, highlighting the strong potential of FeFET-based architectures in neuromorphic and edge computing applications.

In summary, FeRAM technologies are progressing toward greater reliability and scalability through material doping and 3D integration. Ferroelectric resistive memories (FeRRAMs), including memristive devices, have emerged as promising alternatives, offering multilevel conductance control, self-rectifying behaviour, and compatibility with neuromorphic and low-power applications. Meanwhile, FeFETs are advancing toward multifunctional operation by integrating 2D materials and enabling in-memory computing with high-density, multilevel storage capabilities. Collectively, these developments highlight the expanding role of FeNVMs in next-generation memory and intelligent electronic systems.

5.2. Ferroelectric memristor arrays for neuromorphic computing

In addition to conventional FeNVMs, ferroelectric tunnel junctions (FTJs) have emerged as a promising class of memristive devices for neuromorphic computing.[141] FTJs utilize an ultrathin ferroelectric layer sandwiched between two electrodes, where the polarization direction modulates the tunneling barrier and hence the device resistance. This effect, known as tunnel electroresistance (TER), enables analog resistive switching and multilevel conductance states suitable for synaptic weight emulation.[272] As illustrated in Fig. 7(a), when the polarization points toward the electrode with weaker screening (typically M_2), it lowers the average barrier height and increases the tunneling probability, placing the device in a low-resistance (ON) state.[273] Reversing the polarization increases the barrier height and suppresses current flow, switching the device into a high-resistance (OFF) state. The operation of FTJs follows a clear write–polarize–read sequence. A voltage pulse above the coercive field is applied to write the desired polarization direction, effectively programming the resistance state. The resulting polarization state is non-volatile, meaning it remains stable without power. A small read voltage is then used to sense the current without disturbing the polarization, ensuring non-destructive readout. This resistive switching mechanism is attributed to asymmetric electrostatic screening at the ferroelectric/electrode interfaces. Commonly used ferroelectric materials for FTJs include PVDF,[274] $BaTiO_3$,[275,276] $Hf_{0.5}Zr_{0.5}O_2$ (HZO),[36,143,217,277,278] $Pb(Zr,Ti)O_3$ (PZT),[142,279] and $BiFeO_3$ (BFO).[280–282] Combined with excellent scalability and energy efficiency, FTJs are well suited for high-density ferroelectric memristor arrays in brain-inspired computing architectures.[283]

Building on this principle, recent implementations of FTJs have demonstrated not only reliable binary switching but also precise, symmetric multilevel conductance tuning—a key requirement for analog synaptic behaviour. One notable example employs ultrathin PZT tunnel barriers with Ag or Au top electrodes and Nb-doped $SrTiO_3$ as the bottom electrode.[279] By applying a mixed-voltage pulse scheme (MVPS), the device achieves linear and symmetric conductance updates across 256 levels, enabling highly accurate vector-matrix multiplication with minimal error. Fig. 7(b) presents this experimentally realized FTJ array, highlighting its gradual resistance modulation, low write noise, and strong endurance ($>10^9$ cycles). System-level simulations further show that FTJ-based networks can reach a recognition accuracy of $\approx$92% on CIFAR-10, with an inference energy efficiency of $\approx$85 TOPS/W, outperforming conventional memristive systems and underscoring the suitability of FTJs for scalable neuromorphic computing. Beyond accurate and symmetric weight modulation, FTJs have also demonstrated the ability to emulate biological synaptic learning rules. A particularly important example is spike-timing-dependent plasticity (STDP), where the synaptic weight is updated based on the relative timing between pre- and post-synaptic spikes.[280] As illustrated in Fig. 7(c), an FTJ-based synapse based on a $BiFeO_3$ (BFO) ferroelectric barrier can mimic this behaviour through polarization-driven domain dynamics, enabling biologically plausible learning at the device level. In a crossbar network simulation, FTJs were used to form a fully connected spiking neural network that autonomously learned to classify input image patterns—such as vertical, diagonal, and horizontal bars—without external supervision. During training, the synaptic conductance evolved according to STDP rules, and the output neurons specialized in detecting specific patterns. These results highlight the potential of FTJs not only as memory elements but also as plastic, trainable synapses for implementing energy-efficient neuromorphic computing systems. While FTJs demonstrate strong potential for analog switching and synaptic learning, optimizing their behaviour under identical pulse programming (IPP) remains challenging. In particular,

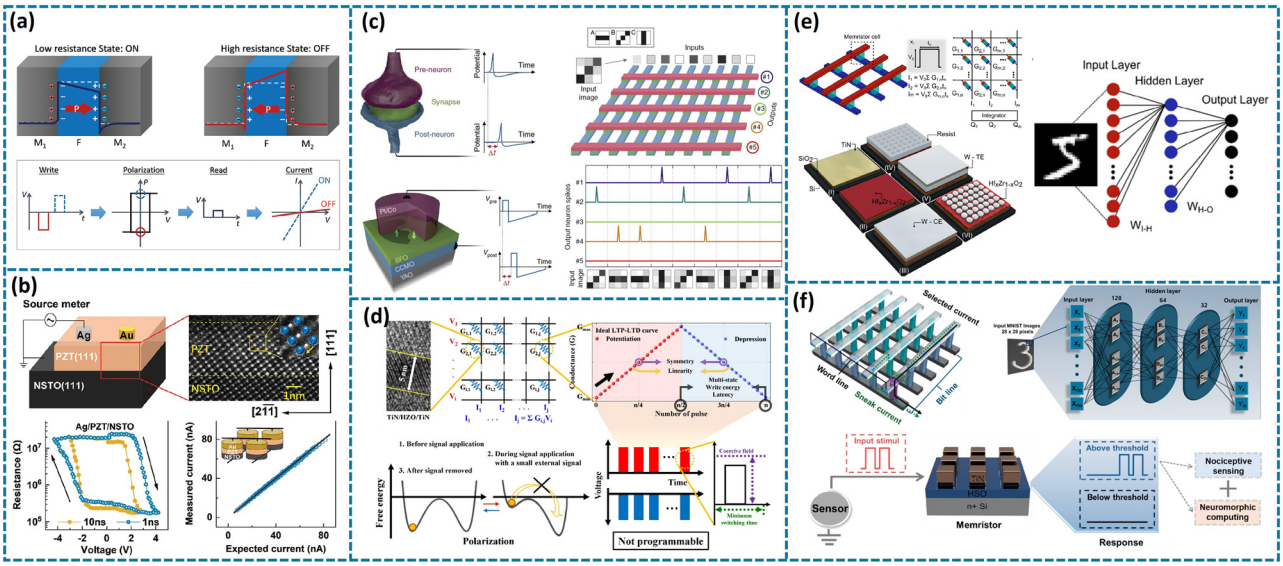

Fig. 7 Ferroelectric tunnel junction (FTJ) devices for neuromorphic computing. (a) Schematic of a ferroelectric tunnel junction (FTJ), where polarization reversal modulates the tunneling barrier and resistance state. Writing is achieved *via* voltage-induced polarization switching; reading is non-destructive and based on tunneling current. Reproduced with permission.[273] Copyright 2019, WILEY-VCH Verlag GmbH & Co. KGaA, Weinheim. (b) Experimental FTJ (Ag/PZT/NSTO) with symmetric, gradual conductance updates under a mixed-voltage scheme; supports high-accuracy vector-matrix multiplication. Reproduced with permission.[279] Copyright 2024, Wiley-VCH GmbH. (c) BFO-based FTJ emulating spike-timing-dependent plasticity (STDP) in a spiking neural network for unsupervised pattern learning. Reproduced with permission.[285] Copyright 2017, The Author(s). Licensed under CC BY 4.0. Published by Springer Nature. (d) Polarization switching dynamics and programming behaviour in TiN/HZO/TiN FTJs under identical pulse programming (IPP); highlights history and continuous effects for multilevel updates. Reproduced with permission.[36] Copyright 2024, The Author(s). Advanced Intelligent Systems published by Wiley-VCH GmbH. (e) Large-scale, selector-free FTJ crossbar array based on $Hf_xZr_{1-x}O_2$ enabling accurate in-memory computing with low sneak path currents. Reproduced with permission.[213] Copyright 2023, The Authors. Advanced Intelligent Systems published by Wiley-VCH GmbH. (f) Integration of FTJs with sensory inputs for threshold-based nociceptive response; demonstrates combined sensing and neuromorphic computation using $HfSiO_x$-based memristors. Reproduced with permission.[284] Copyright 2025, Elsevier B. V.

$Hf_{0.5}Zr_{0.5}O_2$ (HZO)-based FTJs with a TiN/HZO/TiN structure have been studied for their CMOS compatibility and tunable polarization dynamics.[36] As shown in Fig. 7(d), the device's switching behaviour under IPP is influenced by both a history effect and a continuous effect, enabling gradual conductance updates even within a fundamentally bistable free energy landscape. These effects, not captured by traditional LGD or KAI models, allow for multilevel analog programming using optimized sub-coercive pulse schemes, and enable over 5-bit symmetric weight updates suitable for neuromorphic arrays. Building on device-level synaptic behaviours, recent advances have pushed FTJs toward system-level integration for in-memory computing.[213] As shown in Fig. 7(e), a selector-free crossbar array based on a TiN/$Hf_xZr_{1-x}O_2$/W structure was fabricated on a CMOS-compatible Si/SiO_2 platform. These FTJs exhibit more than 60 programmable conductance states with high symmetry, low variability, and strong nonlinearity, enabling precise and energy-efficient vector-matrix multiplication (VMM). Circuit simulations demonstrate that a fully connected neural network mapped to the array achieves up to 92% accuracy on the MNIST dataset, while benefiting from low IR drop and suppressed sneak currents due to the intrinsically low device conductance. This work highlights the potential of FTJs as scalable, backend-integrable building blocks for neuromorphic computing accelerators. Beyond array-level integration, ferroelectric tunnel junctions (FTJs) are now being explored for on-receptor computing, where sensing and computation are co-located at the device level.[284] As shown in Fig. 7(f), an HfSiOx (HSO)-based FTJ integrated with a sensor exhibits threshold-dependent responses, mimicking biological nociceptors that react only when stimuli exceed a critical intensity. The device shows key nociceptive behaviours such as sensitization, relaxation, non-adaptation, and threshold-triggered spiking. These characteristics enable the FTJ to distinguish harmful inputs from benign ones and encode them into neuromorphic signals. Such dual-functionality—combining sensing and computation—opens a new paradigm for intelligent front-end electronics where FTJs serve not only as memory or synaptic elements but also as stimulus-responsive processors for edge AI systems.

6. MEMS micro-speakers and microphones

Piezoelectric MEMS microphones and microspeakers have become key enablers in compact, low-power audio systems, finding applications in consumer electronics, biomedical implants, and robotics. These devices rely on the piezoelectric effect, where mechanical stress generates electric charge (direct effect), and applied voltage induces mechanical deformation (converse effect). In microphones, incoming sound deforms a diaphragm to produce voltage; in microspeakers, electrical signals drive diaphragm motion to emit sound.[150,286] Among the

materials used, aluminum nitride (AlN) is favored for its CMOS compatibility and stability in high-frequency sensing, while lead zirconate titanate (PZT) provides stronger electromechanical coupling, making it suitable for high-output speakers.[146,287] Recent works further introduce structural innovations such as dual-cantilever beams, piston-driven diaphragms, and bimorph stacks, often coupled with sol–gel or aerosol-deposited PZT layers to enhance SPL and reduce distortion. These advancements highlight how material choice and microstructure design jointly drive performance in miniaturized MEMS acoustic devices. In addition to SPL and THD, frequency response characteristics and conversion efficiency have become critical supplementary metrics in evaluating acoustic performance comprehensively, further enhancing the design and optimization of MEMS-based audio solutions.

Among these, bioinspired directional sensing (Fig. 8(a)) leverages the mechanically coupled diaphragms of Ormia ochracea to enable broadband sound localization in a compact aluminum nitride (AlN)-based piezoelectric MEMS microphone, ideal for auditory prosthetics and surveillance applications.[152] Its frequency response remains consistent from 1 kHz to 10 kHz, ensuring broad auditory capture. In contrast, Fig. 8(b) illustrates a clinically oriented floating piezoelectric microphone mounted on the human incus, utilizing a ceramic bimorph element for effective signal pickup in totally implantable cochlear implants (TICIs), offering improved sensitivity and hygiene advantages over conventional external microphones.[151] The microphone achieves a flat frequency response between 0.3 and 10 kHz and sensitivity of 0.8 mV Pa^{-1} at 1 kHz under 10 Vpp excitation. The measured efficiency of the microphone is approximately 0.9%, balancing output voltage and mechanical robustness. Fig. 8(c) demonstrates the integration of MEMS microphones in a robotic auditory system. Four MEMS microphones are mounted on a humanoid robot's head to capture spatially separated audio inputs for sound source localization. The microphones, based on piezoelectric sensing principles though without specified material in the study, collect audio data as a TurtleBot3 mobile robot provides ground-truth position tracking. Deep learning models including convolutional neural networks (CNN), LSTM, and biLSTM are trained to estimate 2D spatial coordinates of the sound source based on wavelet-transformed acoustic inputs. The system enables accurate real-time auditory perception, even in the presence of movement or noise, and highlights the potential of MEMS microphones combined with AI for human–robot interaction and intelligent environmental awareness.[288] Each MEMS unit demonstrated a frequency range between 500 Hz and 8 kHz, which is sufficient for human voice detection and localization tasks. These sensing-side innovations are complemented by the development of advanced MEMS microspeakers, as illustrated in Fig. 8(d)–(f), each tackling unique challenges in bandwidth, distortion, and integration. Fig. 8(d) introduces a piezoelectric MEMS microspeaker design based on dual triangular cantilever diaphragms optimized for multi-mode acoustic actuation. One diaphragm targets low-frequency responses while the other handles higher frequencies, with both integrated into a common structure using PZT (lead zirconate titanate) thin films

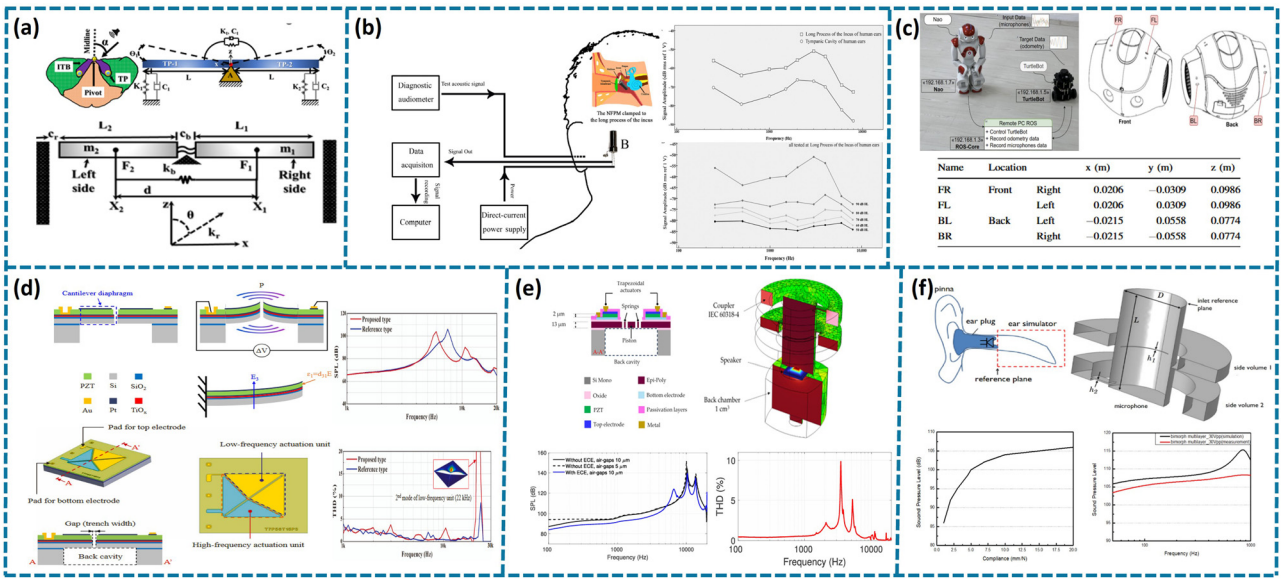

Fig. 8 MEMS micro-speakers and microphones. (a) Schematic illustration of a directional MEMS microphone inspired by the Ormia ochracea fly, featuring mechanically coupled diaphragms. Reproduced with permission.[152] Copyright 2020, PMC. (b) Schematic setup of a humanoid robot head equipped with four MEMS microphones for deep-learning-based sound source localization. Reproduced with permission.[151] Copyright 2022, Springer Nature. (c) Schematic diagram of a floating piezoelectric microphone mounted on the human incus for fully implantable middle-ear systems. Reproduced with permission.[288] Copyright 2023, Wiley. (d) Schematic structure of a dual-cantilever piezoelectric MEMS microspeaker with asymmetric diaphragm structures for multi-mode actuation. Reproduced with permission.[147] Copyright 2024, Elsevier. (e) Schematic configuration of a piston-type piezoelectric MEMS microspeaker actuated by trapezoidal PZT plates through folded springs. Reproduced with permission.[149] Copyright 2023, IEEE. (f) Schematic configuration of a multilayer bimorph MEMS microspeaker evaluated in an ear canal simulator for enclosed-field acoustic analysis. Reproduced with permission.[148] Copyright 2025, MDPI.

and metallic electrodes. Finite element modeling reveals that asymmetric geometries help balance stress and displacement, reducing nonlinearities and minimizing total harmonic distortion (THD). Experimental results confirm broadband sound pressure level (SPL) enhancement across the 5–13 kHz range. This design addresses key limitations of single-mode MEMS speakers by enabling more faithful audio reproduction at low driving voltages, suitable for earbuds, smart wearables, and hearing aids.[147] Additionally, the dual-mode structure achieves a flatter frequency response from 1 kHz to 12 kHz and reaches a conversion efficiency of 10.2% at 9.8 kHz, providing a stronger overall performance profile compared to conventional unimodal devices. Pushing the limits further toward high-fidelity and compact design, Fig. 8(e) presents the design and evaluation of a full-range piezoelectric MEMS microspeaker, which employs a 2 μm thick sol–gel PZT layer embedded between patterned electrodes on four trapezoidal plates, which are mechanically linked to a central piston *via* folded elastic springs. This configuration enables synchronized motion of the actuators and piston, maximizing effective acoustic area while maintaining an acoustically closed behaviour through engineered air gaps and a dedicated back chamber. The speaker achieves SPL values exceeding 107 dB above 500 Hz under 30 Vpp excitation, with total harmonic distortion (THD) remaining below 1% at 1 kHz. Both numerical simulations and experimental results using an IEC 60318-4 ear simulator confirm the linear mechanical response and high-fidelity sound reproduction, even without the aid of polymeric sealing membranes. This robust and compact design, with a footprint of 4.5×4.5 mm^2, demonstrates significant promise for future integration into miniaturized in-ear audio devices.[149] System-level measurements show a nearly flat SPL curve from 500 Hz to 10 kHz, with conversion efficiency peaking at 13.1% around 4.3 kHz, indicating strong performance in both voice and music frequency bands. To validate system-level performance in realistic acoustic environments, Fig. 8(f) presents the acoustic testing of a packaged multilayer bimorph MEMS speaker inside an artificial ear canal based on the IEC 60318-4 standard. The speaker employs aerosol-deposited PZT layers over a stainless-steel substrate, forming a robust and compact structure. Measurement and simulation results reveal that the speaker maintains a flat frequency response and achieves SPL over 108 dB at 1 kHz under 30 Vpp, while preserving low distortion. The diaphragm's edge compliance is shown to be a critical factor in output efficiency, and the entire structure demonstrates strong potential for woofer-type integration in in-ear systems. Efficiency analysis confirms an acoustic conversion efficiency of 9.5% at 1 kHz, which is competitive among MEMS woofer-type designs. Such devices meet the rising demand for miniaturized, high-output audio modules in consumer electronics and medical audio delivery.[148]

Overall, these designs showcase the flexibility of piezoelectric MEMS structures in tailoring acoustic performance through structural geometry and material selection. Whether using AlN for CMOS compatibility or PZT for high-sensitivity applications, these devices demonstrate how MEMS integration and material engineering together enable miniaturized, high-performance acoustic systems.

7. Reconfigurable photonic devices: acousto-optic and electro-optic control

Piezoelectric and ferroelectric materials play a pivotal role in reconfigurable photonic devices by enabling efficient acousto-optic[48,61,66,153–176] and electro-optic[178–185] modulation. Through mechanical vibrations or electric-field-induced refractive index changes, these materials facilitate dynamic control of optical signals—such as frequency shifting, phase tuning, and amplitude modulation—crucial for integrated photonic circuits in communication, sensing, and optical computing applications.

7.1. Acousto-optic modulators

In the study of piezoelectric actuated acousto-optic modulation, achieving efficient microwave-to-optical transduction relies on precise multi-physical-field coupling control to enable cross-frequency information transfer and efficient energy conversion. The mode-coupling framework illustrated in Fig. 9(a) provides a systematic theoretical perspective for analyzing and optimizing the synergistic interactions among microwave, mechanical, and optical modes. This system comprises four fundamental components: microwave mode, mechanical mode, signal optical mode, and pump optical mode.[66] Under microwave excitation, the piezoelectric effect induces high-frequency mechanical oscillations, generating propagating acoustic waves. These waves travel within the piezoelectric material and interact with localized optical modes, thereby establishing a cross-spectral information transmission pathway. Specifically, the microwave mode is coupled into the system *via* an impedance-matched port, characterized by an external coupling rate Γ_{ex} and intrinsic loss Γ_i. Concurrently, the piezoelectric transduction mechanism converts microwave energy into mechanical vibrations, leading to the formation of an acoustic mode with frequency Ω_m, governed by the electromechanical coupling strength g_{em}. The interaction between the mechanical mode and optical modes constitutes the core dynamical mechanism of this system. The signal optical mode, modulated by the optomechanical coupling rate g_{om}, undergoes optical field modulation *via* mechanical oscillations, facilitating effective signal transmission and modulation.[289] A pump optical mode can be introduced to enhance overall modulation efficiency through nonlinear scattering or parametric amplification, maintaining a high photon population density and further improving the stability and tunability of the optical signal. The intrinsic losses $\kappa_{o,i}$ and external coupling rates $\kappa_{o,ex}$ of both optical modes collectively determine the system's total optical quality factor, thereby influencing photon lifetime and optical resonance characteristics.

Different acoustic modes affect the electroacoustic coupling factor and the electro-optic coupling factor through stress distribution, thereby determining the modulation efficiency

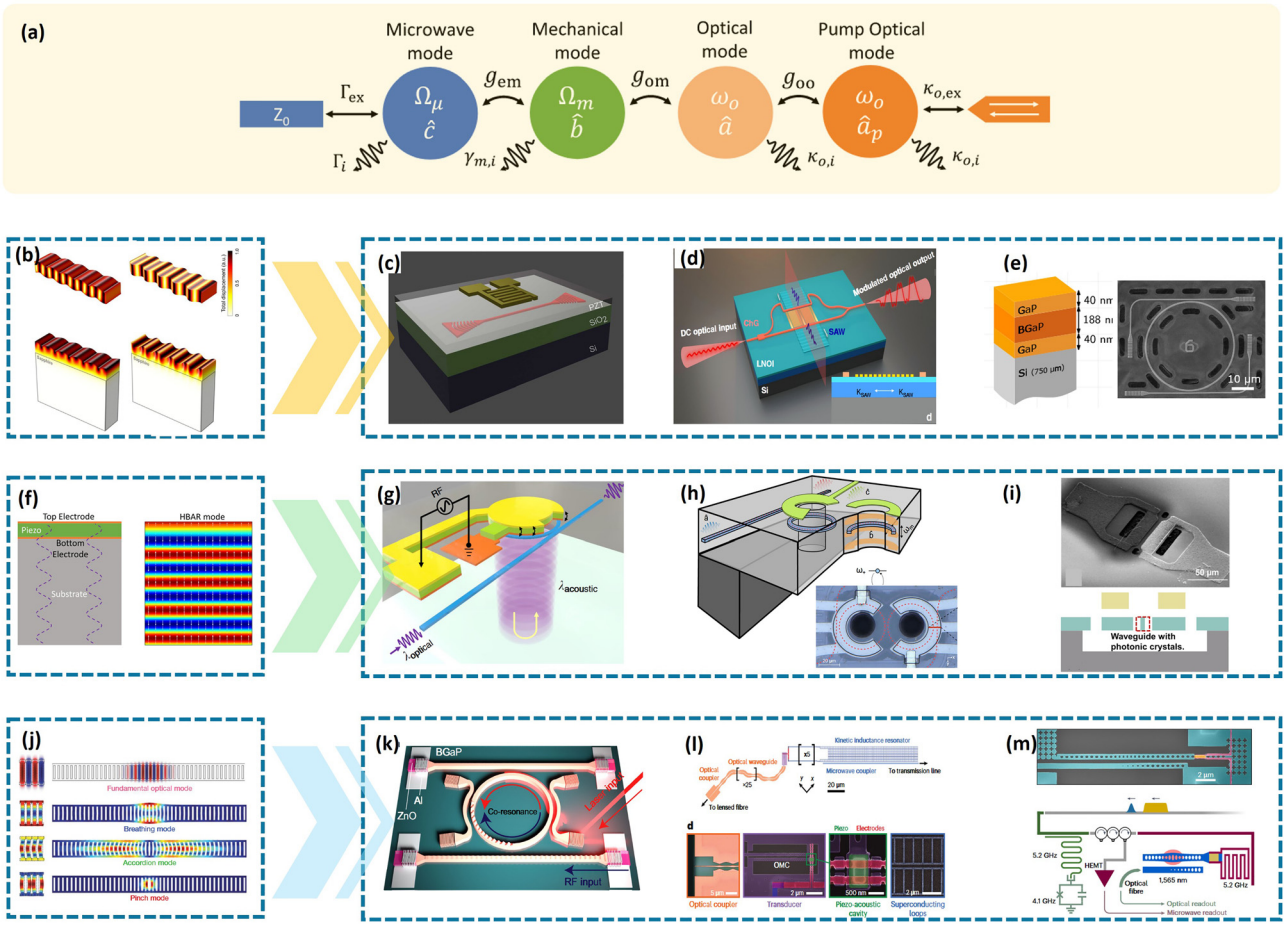

Fig. 9 Piezoelectric actuation device for AO modulation. (a) Mode coupling scheme for microwave-to-optical transduction. Reproduced with permission.[66] Copyright 2024, The Optical Society. (b) Total displacement profiles of typical acoustic waves actuated for microwave-optical interface, showing Rayleigh–Lamb and Love-type shear modes on suspended and bulk substrate. Reproduced with permission.[61] Copyright 2021, The Optical Society. (c) An IDT-enabled microwave-optical interface utilizing an Si waveguide embedded between a PZT layer and SiO_2 cladding. Reproduced with permission.[48] Copyright 2022, American Chemical Society. (d) A SAW-based microwave-optical interface with an MZI waveguide on $Ge_{25}Sb_{10}S_{65}$ film atop LNOI. Reproduced with permission.[292] Copyright 2025, Springer Nature. (e) AO frequency shifter with GaP–BGaP–GaP hetero-structure device with optical resonator exhibits inherent quality factors higher than 25 000 and 20 000, operating at optical phase-matching conditions. Reproduced with permission.[293] Copyright 2023, Wiley-VCH. (f) Cross-sectional view of a BAW resonator illustrating the longitudinal displacement distribution of a typical HBAR mode. Reproduced with permission.[66] Copyright 2024, The Optical Society. (g) A high modulation speed acousto-optic modulation achieved on photonic integrated chips by stimulating high-harmonic body acoustic wave resonance. Reproduced with permission.[160] Copyright 2020, Springer Nature. (h) A piezoelectrically actuated photonic–microwave transducer with HBAR acoustic modes in a suspended cladding coupling to a microwave line and DC stress-optic tuning. Reproduced with permission.[156] Copyright 2024, The authors. (i) A metal–air–piezoelectric thin-film configuration, incorporating air gaps and suspended structures, enables enhanced acoustic wave propagation control and improved acousto-optic coupling efficiency for high-frequency applications. Reproduced with permission.[294] Copyright 2024, IEEE. (j) Optomechanical crystal design, showing optical and mechanical modes FEM simulation. Reproduced with permission.[155] Copyright 2009, Springer Nature. (k) An optomechanical ring resonator with integrated photonic and phononic waveguides, supporting co-resonant photon and phonon modes. Reproduced with permission.[167] Copyright 2023, Springer Nature. (l) Schematic of the suspended optical waveguide feeding the piezo-optomechanical transducer with electrical terminals, which are connected to the microwave kinetic inductance resonator. Reproduced with permission.[162] Copyright 2024, Springer Nature. (m) A piezo-optomechanical transducer with a piezoelectric block embedded in a superconducting resonator alongside an optomechanical photonic-crystal cavity, allowing microwave pulses to drive a fixed-frequency qubit, and its readout signal is upconverted to the optical domain *via* the transducer. Reproduced with permission.[164] Copyright 2025, Springer Nature.

and mode matching effect. This suggests that acoustic design in the design of AOM devices will be beneficial for achieving efficient broadband modulation. Guided by this, the excitation and propagation of acoustic modes directly determine modulation efficiency. In bulk substrates, the Rayleigh-type surface acoustic wave (SAW) mode induces elliptical particle motion confined within a shallow surface region, making it suitable for near-field coupling. Recognizing these limitations of Rayleigh-type surface waves, researchers have turned to suspended Lamb modes and Love-type shear-horizontal waves as complementary solutions. The symmetric S0 branch offers minimal attenuation but a narrower operational band, whereas the antisymmetric A0 branch extends bandwidth at the cost of higher bending-induced loss. Love-type shear-horizontal waves introduce

strong shear confinement that suppresses crosstalk, thereby enabling higher integration density. Although all three rely on piezoelectric transduction, they differ in vertical energy distribution and modal field overlap, providing designers with explicit trade-offs between low loss, wide bandwidth, and compact.[61,290]

As illustrated in Fig. 9(b), the displacement distributions of Rayleigh, Lamb, and Love waves reveal distinct propagation and spatial confinement characteristics. These diverse modes expand the design space in frequency selectivity, bandwidth tunability, and energy localization, offering the material and structural foundation for high-performance, low-loss, and compact acousto-optic modulators (AOM). Building on this modal analysis, device designs exploit interdigital transducer (IDT) finger period and electrode placement to. Selectively excite SAW, Lamb, or shear-horizontal modes. In bulk resonator configurations such as high-overtone bulk acoustic resonators and film bulk acoustic resonators, the Fabry–Perot cavity formed by electrodes and substrate thickness supports longitudinal or shear bulk modes with high quality factors. Surface-wave and bulk-wave modulators both rely on geometric and piezoelectric-layer optimization to achieve optimal coupling and frequency response. The construction of high-Q mechanical resonant cavities or the adoption of cavity-enhanced strategies can prolong the lifetime of mechanical modes and strengthen their interaction with optical modes. Furthermore, the integration of multi-mode optical cavities, combined with pump-enhanced photon number amplification, contributes to increased acousto-optic conversion gain. Combined with structural engineering techniques such as film suspension,[158,171,172,291] these strategies provide precise control over acoustic pathways and acousto-optic interaction regions, enabling device operation across the RF and millimeter-wave regimes.

Building on the mode-coupling framework that links electromechanical coupling strength and acoustic confinement to modulation efficiency, device designs translate key theoretical parameters into practical geometries. Specifically, the IDT finger period is chosen to satisfy the phase-matching condition for the targeted acoustic mode, while electrode overlap and port impedance are tuned to achieve the desired external coupling rate and minimize intrinsic loss By mapping the coupling coefficients g_{em} and g_{om} onto IDT geometry and electrode positioning, designers can optimize classic piezoelectric-based modulators for high conversion efficiency and bandwidth.[48] In these devices, metallic IDTs patterned on PZT thin films generate in-plane acoustic waves that remain confined near the surface and couple into adjacent optical waveguides, as shown in Fig. 9(c). The efficiency of this transduction is quantitatively characterized by the parameter $V\pi L$, which reflects the voltage–length product required to induce a phase shift of π in the optical signal. Experimental implementations have demonstrated gold and aluminium IDTs operating at 576 MHz and 2 GHz, respectively, with corresponding $V\pi L$ values of 3.35 V cm and 3.60 V cm, indicating moderate modulation efficiency governed by the coupling coefficient g_{em} and the g_{om} for opto-mechanical interaction.

It is important to note that SAWs are primarily confined to the surface of the piezoelectric layer, with their acoustic modes decaying exponentially into the underlying substrate.[157] Therefore, in integrated designs, the placement of optical waveguides must be carefully optimized to maximize acousto-optic overlap. Generally, a suspended piezoelectric layer design can enhance the acoustic quality factor and modulation efficiency, although it introduces greater fabrication complexity.[158,161,163] Fig. 9(d) presents the non-suspended hybrid approach that employs an LNOI platform with integrated $Ge_{25}Sb_{10}S_{65}$ thin-film Mach–Zehnder interferometers to leverage both the high modulation efficiency on lithium niobate substrate and the pronounced nonlinear response of chalcogenide glass.[292] Under this scheme push–pull modulation at 0.84 GHz achieves an exceptionally low $V\pi L$ of 0.03 V cm while maintaining mode efficiency comparable to suspended structures. Fig. 9(e) presents a boron-doped gallium phosphide heterostructures on silicon that combine lattice-matched epitaxial growth with strong piezoelectric coupling to form a scalable AOM platform.[293] In this design of SAW-based optical modulator, the electrodes and substrate thickness form an acoustic Fabry–Pérot cavity that supports longitudinal and shear bulk modes with high Q factors near 1 GHz on bulk substrate, fully exploiting the opportunity brought by functional piezoelectric materials that reach both fabrication accessibility and device optimum performance. Collectively, these designs share the need for precise IDT period tuning and electrode placement to optimize the overlap integral and coupling strength. Film suspension and integration of novelly developed materials can further enhance acoustic confinement, quality factor, bandwidth tunability, and modulation efficiency.

Another pathway for the stronger acousto-optic interaction and highly integrated design of acousto-optic modulators by employing BAW modalities. Fig. 9(f) illustrates the longitudinal displacement distribution under a typical HBAR mode, where acoustic waves form standing waves across the multilayer stack in the vertical direction, thereby exciting multiple higher-order harmonic modes. Unlike SAW devices, which rely on in-plane surface propagation, the longitudinal wave of HBAR's vertical confinement of acoustic energy makes it especially well-suited for three-dimensional vertical integration platforms. Fig. 9(f) illustrates the HBAR longitudinal displacement distribution where vertically confined standing waves excite higher-order harmonics. Unlike SAW, this vertical confinement supports an acoustic quality factor Q that directly reflects the ratio of energy stored in the mechanical mode to the intrinsic loss defined in the multimode model. By minimizing energy loss through vertical energy trapping while maintaining adequate external coupling efficiency *via* electrode and cavity design, HBAR AOMs achieve high Q without enlarging the chip footprint.[160] In this design, the transverse stress of BAW with large shear stress can also be demonstrated for AO modulation by placing the optical waveguide at the opposite node of the stress distribution on the LN substrate.[159] Such a balance between intrinsic loss and external coupling underpins both their broad bandwidth and efficient microwave-to-optical transduction.

Fig. 9(g) further demonstrates HBAR's capacity to excite high-order bulk wave harmin onics, underscoring its potential for high-speed modulation. Such architectures have been successfully implemented on Si_3N_4 waveguide platforms. Silicon nitride is prized for its ultralow optical propagation loss and strong Kerr nonlinearity. However, intrinsic Si_3N_4 lacks a Pockels effect, making direct high-speed electro-optic modulation challenging. To address this, researchers have integrated HBAR structures within photonic-crystal stacks, harnessing their strong acousto-optic coupling to achieve modulation at microwave frequencies above 1 GHz. The vertical confinement of acoustic modes not only liberates lateral design freedom and reduces modal crosstalk but also ensures outstanding modulation performance while maintaining low optical loss.[160,293] This hybrid HBAR nanophotonic platform holds promise for frontier applications such as synthetic-dimension topological photonic devices, on-chip microwave-to-optical transducers, and low-phase-noise optoelectronic oscillators. For example, a demonstration isolator on Si_3N_4 achieved over 17 dB of isolation *via* HBAR-induced spatiotemporal modulation. Then the integrated HBAR–nanophotonic platform in Fig. 9(h) combines a locally suspended SiO_2 cladding layer with microwave coupling and electrostatic tuning to yield a photon transduction efficiency of 1.6×10^{-5} and a 25 MHz modulation bandwidth under a 21 dBm drive without superconducting elements.[156] Another BAW-based modulator design in Fig. 9(i) implies a metal–air–piezoelectric architecture to introduce dual suspension and sacrificial air gaps to isolate the acoustic core, suppress damping, and demonstrate excitation of the A1 Lamb mode at 10.38 GHz with a high electromechanical coupling coefficient of 28%.[294] Overall, these implementations illustrate that precise vertical confinement and modal overlap control enable highly integrated, high-performance acousto-optic modulators across diverse material platforms.

While classical SAW and BAW modulators employ extended interaction regions and rely on macroscopic interdigital transducer designs, emerging quantum acousto-optic devices must instead confine both photons and phonons within sub-cubic-micron volumes to meet stringent requirements for coherence, noise suppression, and nonclassical state transduction. Fig. 9(j) presents a typical OMC structure where finite element simulations demonstrate the co-localization of optical and acoustic modes.[155] In this scheme the periodic phononic and photonic crystals create band gaps that confine photons and phonons to the same sub-cubic-micron region, thereby maximizing the optomechanical coupling rate while suppressing intrinsic loss Unlike classical AOM devices where surface acoustic waves propagate over large interaction regions with substantial energy dissipation, OMC-based quantum AOMs exhibit higher interaction strength and reduced parasitic modes due to this tight spatial confinement.

Another critical requirement for quantum-level performance is the suppression of thermal noise, which directly influences coherence, signal fidelity, and the detection of single-photon events. In classical SAW and BAW modulators, thermal phonon populations introduce excess noise, particularly when the interaction volume is large and the device is operated at room temperature. By contrast, OMC-based devices can be engineered to minimize mechanical dissipation and heat generation, leveraging phonon band gaps to filter thermal excitations and thereby reduce noise contributions. This low-noise environment not only improves the stability of quantum transduction but also reduces the actuation energy required to achieve strong modulation.

Building on the multimode coupling principle, both optomechanical ring resonators and piezo-driven optomechanical crystals are designed to co-localize optical and acoustic modes, enabling efficient microwave-to-optical conversion with minimal energy loss. Fig. 9(k) illustrates an optomechanical ring resonator (OMR) optimized for efficient microwave-to-optical frequency conversion.[167] By confining photons and phonons within co-resonant cavities, the optical quality factor of 10^5 and the acoustic quality factor of 10^3 can be interpreted as the direct manifestation of low intrinsic loss and strong coupling coefficients g_{em} and g_{om} defined in the multimode framework. At an acoustic pump power of 1.6 mW, the OMR achieves an internal conversion efficiency exceeding 2 percent, which corresponds to a high ratio of coherent transduction to total loss channels and validates the role of traveling-wave coupling in maximizing external coupling rate Γ_{ex} while suppressing unwanted parasitic modes. Compared to traditional standing-wave cavities, the traveling-wave nature of the ring resonator supports multimode coupling, multi-channel conversion, and flexible integration into large-scale OMIC networks. Compared to such OMR structures, the hybrid piezoelectric–optomechanical devices illustrated in Fig. 9(l) extend this concept to quantum transduction. Extending this principle, the hybrid piezoelectric–optomechanical transducer in Fig. 9(l) demonstrates non-classical photon pair generation with a heralding efficiency of up to 47%.[162] This metric can be viewed as a measure of coherent coupling efficiency between the mechanical mode and both microwave and optical ports, and its improvement from 40% to 80% fidelity reflects the reduction of microwave loss and enhanced phase-matching between the optical k_o and acoustic Ω_m modes. The system leverages spontaneous parametric down-conversion combined with piezoelectric-driven optomechanical coupling to achieve entanglement across frequency domains.

In Fig. 9(m), a fully integrated piezo-optomechanical transducer achieves single-shot optical readout of a superconducting qubit with 81 percent fidelity while converting microwave signals near 5.2 GHz to optical frequencies around 191 THz.[164] This performance can be interpreted within the multimode coupling model because of precise control of $\kappa_{o,i}$, Γ_{ex}, and g_{om}, enabling high signal-to-noise conversion under cryogenic operation. Collectively, these quantum-oriented OMC devices translate the abstract coupling parameters into practical performance metrics, including conversion efficiency, heralding probability, and readout fidelity, to establish a clear design link between classical AOM principles and quantum acousto-optic transduction.

Modulation efficiency, typically expressed by the $V\pi L$ parameter, remains a primary metric for assessing the performance

of the AOM device. To enhance this efficiency, structural adaptations such as released or suspended configurations are often employed, as these lower $V\pi$ by increasing acousto-optic coupling, thereby enabling reduced drive voltages without compromising bandwidth. SAW platforms benefit from optimized IDT designs and differential acoustic paths that suppress energy leakage, while HBAR resonators rely on vertical acoustic confinement to maintain high optical Q factors. In contrast to the classical implementations, OMC architectures realize strong optomechanical coupling by confining both optical and mechanical modes within deeply subwavelength volumes, enabling efficient modulation under low power and low thermal occupancy. The fundamental shift in design philosophy is evident when comparing IDT-based SAW and BAW AOMs to quantum-oriented OMC architectures, as the former emphasize fabrication maturity and device generality, whereas the latter demand spectral precision, mode purity, and nonlinear coupling capabilities tailored to non-classical state generation and transduction. Consequently, the hybridization of OMC structures with piezoelectric excitation emerges as a critical strategy in the development of piezoelectric transducers for advanced modulation, offering synergistic enhancement in both signal fidelity and thermal noise suppression, which are indispensable for large-scale quantum networks and cryogenic quantum processors. The intrinsic photoelastic effect links material refractive index modulation to the cube of the index, which means that high-index waveguides such as silicon, or the integration of transducers fabricated on materials with large piezoelectric coefficients, including PZT and ScAlN, significantly improve tuning efficiency and reduce power consumption.

Emerging materials have further expanded the AOM material toolbox. ScAlN films prepared by sputtering or metal–organic chemical vapor deposition (MOCVD),[166] exhibit stronger piezoelectric response and better mode overlap than AlN, though etching challenges remain at high scandium concentrations.[154] $BaTiO_3$ (BTO) combines strong electro-optic and piezoelectric properties, enabling modulators with bandwidths approaching 30 GHz, yet its piezoelectric-driven potential for AOM applications is still underexplored.[165,168] Recent studies on silicon–hafnium beryllium oxide hybrid micro-ring devices show that the hafnium beryllium oxide layer functions as both an active optical medium and a piezoelectric actuator, achieving bidirectional tuning with power efficiency as low as 0.12 nW pm^{-1}.[169] In addition, potassium sodium niobate (KNN) offers a high piezoelectric strain coefficient, suggesting potential for lead-free AO modulation and energy-harvesting applications.[95]

From the perspective of SAW-based AOMs, ongoing development emphasizes enhancing acousto-optic coupling by adopting high-performance substrates such as X-cut $LiNbO_3$ and ScAlN. These materials offer strong piezoelectricity, efficient mode overlap with optical waveguides, and support low-loss, phase-matched excitation for surface waves. For BAW-based devices, the current focus lies in fabricating high-Q resonators with vertical confinement and multilayer heterostructures that achieve high acoustic velocity contrast and efficient GHz-class modulation. OMC-based AOMs, by contrast, represent the frontier of nanoscale photon–phonon interaction, where co-localized optical and mechanical fields enable exceptionally strong coupling suitable for both classical signal processing and quantum transduction. Integration of piezoelectric elements with OMCs allows efficient phonon generation and manipulation at GHz frequencies, which is particularly relevant for linking superconducting qubit systems through photonic networks.[153]

Looking forward, low-power and high-speed integration across SAW, BAW, and OMC platforms will depend on breakthroughs in piezoelectric actuator engineering, material growth and patterning precision, and scalable heterogeneous integration. A synergistic approach that combines the advantages of this modulation of cross-frequency mode-coupling architectures is essential for developing programmable RF-optical compatible systems and quantum-compatible AOM devices.

7.2. Electro-optic tunable waveguides

Electro-optical (EO) tunable waveguides are essential components in modern photonic integrated circuits (PICs).[182–184] By applying an external electric field, the refractive index of an EO material can be modulated, leading to phase shifts and amplitude changes in guided optical modes. This mechanism allows for high-speed and broadband modulation with low insertion loss, which is critical for optical communication systems, signal processing, and emerging applications in photonic computing. Various materials such as lithium niobate ($LiNbO_3$, LN), barium titanate ($BaTiO_3$, BTO), and lead zirconate titanate (PZT) have been employed for EO tuning, integrated either monolithically or as hybrid layers onto silicon or silicon nitride waveguides. These configurations facilitate scalable and reconfigurable photonic architectures, advancing programmable photonic systems for next-generation technologies.

Fig. 10(a) shows an LN-based EO modulation device based on a Mach–Zehnder interferometer (MZI) with multiple branches for in-phase (I) and quadrature (Q) signal modulation, achieving a 3 dB bandwidth larger than 70 GHz.[185] Fig. 10(a) illustrates the layout of the device, which features an input grating coupler, a multimode interference (MMI) splitter, and distinct I and Q branches controlled by thermo-optic (TO) phase shifters. Ground-signal-ground (GSG) electrodes are integrated along the branches to apply the required external voltages for EO modulation, and grating couplers at the output end couple light off-chip. The optical modulation response is characterized by measuring the normalized transmission as a function of the applied voltage. Fig. 10(b) shows the transmission curves of the I and Q branches, indicating clear sinusoidal modulation behaviour. The half-wave voltages ($V\pi$) are extracted for devices of different lengths: 1.9 V for a 13-mm-long device and 3.1 V for a 7.5-mm-long device. The extinction ratio (ER) exceeds 25 dB, indicating a strong modulation contrast. The variation of transmission with voltage demonstrates that the applied electric field modifies the refractive index of the EO material *via* the Pockels effect, resulting in phase shifts and thus modulation of the transmitted light intensity. The transmission peak shifts correspond to the phase

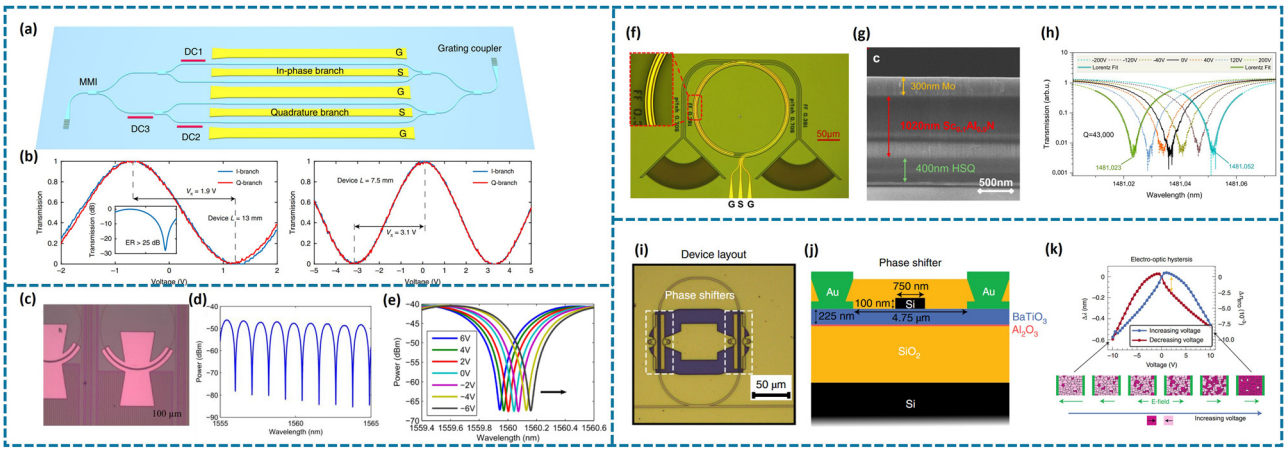

Fig. 10 Electro-optic tunable waveguides. (a) Schematic of an LNOI-based *IQ* modulator. (b) Normalized optical transmission of both branches of the 13-mm and 7.5-mm devices as a function of the applied voltage, showing $V\pi$ of 1.9 V and 3.1 V, respectively. The inset shows the measured normalized transmission on a logarithmic scale, showing an extinction ratio greater than 25 dB. (a) and (b) reproduced with permission.[185] Copyright 2022, Springer Nature. (c) Microscope picture of the PZT-on-SiN ring resonator with gold contacts. (d) Transmission spectrum of the PZT-on-SiN ring resonator (waveguide width = 1 μm, radius = 150 μm). (e) Ring transmission as a function of applied DC voltage, the arrow shows in which order the spectra is measured. (c)–(e) reproduced with permission.[295] Copyright 2017, Optical Society of America. (f) Microscope image of a $Sc_{0.1}Al_{0.9}N$ EOM device. Insect: Zoomed-in view of the GSG electrodes illustrating good alignment with the buried ring resonator. (g) Cross-sectional SEM image of bonded ScAlN-on-insulator substrate. (h) Transmission spectra of a near-critically coupled TE-mode resonance under different applied voltages. Lorentzian fits for ±200 V are shown in bold. (f)–(h) reproduced with permission.[178] Copyright 2024, Springer Nature. (i) Micrograph of a racetrack resonator device with BTO phase shifters (dashed rectangles). (j) Schematic cross-section of the phase shifter, consisting of a silicon ridge waveguide on top of a BTO layer with gold electrodes. (k) Top: resonance shift as a function of increasing and decreasing voltage (butterfly-shaped curve), yellow arrow indicates the range of stable domain states at 2 V bias. Bottom: Schematics indicating how domains are populated while increasing the voltage applied between the electrodes indicated in green. (i)–(k) reproduced with permission.[180] Copyright 2022, Springer Nature.

modulation, with a π phase shift achieved at $V\pi$, and the direction of the shift depends on whether the refractive index increases or decreases under the applied field. Besides, Alexander *et al.* demonstrated an integrated photonic modulator based on PZT deposited on silicon nitride (SiN) waveguides. Fig. 10(c) shows the fabricated ring resonator structure with PZT coating and gold electrodes for modulation control.[295] The device was fabricated on LPCVD SiN waveguides with a high-quality PZT layer deposited by chemical solution deposition (CSD), patterned using reactive ion etching (RIE) for precise electrode placement. The transmission spectrum of the ring resonator, shown in Fig. 10(d), exhibits a series of resonance dips corresponding to different wavelength channels, confirming the *Q*-factor of 3000 and well-defined resonance characteristics of the structure. The free spectral range (FSR) measured was approximately 1.11 nm, with a waveguide width of 1 μm and ring radius of 150 μm. Fig. 10(e) shows the EO modulation performance, where the ring transmission is plotted as a function of wavelength under different applied voltages. The resonance wavelength shifts with applied voltage, demonstrating a tuning efficiency of approximately 17.2 pm V^{-1}, and a $V\pi L\pi$ of about 1 V cm. The device also exhibited a modulation bandwidth exceeding 25 GHz and optical loss below 1 dB cm^{-1}. This work demonstrates the potential of PZT-on-SiN platforms for high-speed and low-loss integrated photonic modulators. Another work also employed ring structure but with a different material. As shown in Fig. 10(f), Yang *et al.* fabricated micro-ring resonators (MRR) on scandium-doped aluminum nitride (ScAlN)-on-insulator substrates.[178] The cross-sectional SEM image in Fig. 10(g) highlights the ScAlN waveguide and electrode structure that ensures strong overlap between the optical mode and the applied electric field. The experimental transmission spectrum in Fig. 10(h) shows resonance shifts under varying applied voltages, indicating an effective tuning mechanism through the Pockels effect. The measured *Q*-factor exceeded 43 000, and the device showed a notable shift in transmission spectra, confirming enhanced EO performance in ScAlN. This platform offers a scalable and CMOS-compatible path for high-speed photonic modulators and phase shifters.

Beyond EO modulators, materials that exhibit intrinsic ferroelectric properties can be used for non-volatile memory in integrated photonic circuits. As shown in Fig. 10(i), Geler-Kremer *et al.* designed a phase shifter consisting of a silicon ridge waveguide integrated on top of a BTO thin film, encapsulated within multilayer stacks including Al_2O_3 and Au electrodes.[180] The cross-sectional schematic in Fig. 10(j) illustrates the device layers, including a 100-nm Si waveguide core, 225-nm buffer, and 750-nm phase shifter section atop the BTO layer. The electro-optic hysteresis measurement in Fig. 10(k) demonstrates multilevel, non-volatile phase control, with eight distinct states achieved through controlled ferroelectric domain switching. The device exhibits ultralow insertion loss (~0.07 dB) and switching energy as low as 4.6–26.7 pJ, offering a scalable solution for programmable photonic circuits.

While significant progress has been made across multiple EO material platforms, several opportunities remain under-explored. For instance, phase-change ferroelectrics like potassium sodium niobate (KNN) or EO-active III–V semiconductors

(*e.g.*, GaP, GaAs) could offer higher bandwidth and better quantum-optic integration than current platforms. Moreover, exploring GHz–THz modulation regimes, quantum-classical cross-over dynamics and integration with superconducting or spintronic systems could unlock novel applications in quantum photonics and photonic neuromorphic computing. In conclusion, future research should focus not only on optimizing device figures-of-merit ($V\pi$, Q, bandwidth, energy) but also on identifying and engineering materials that bridge classical and quantum functionality in compact, low-power platforms.

8. Conclusions

The convergence of piezoelectric and ferroelectric effects in MEMS and NEMS platforms has opened a versatile pathway toward building multifunctional micro/nano-devices capable of sensing, actuation, memory storage, and signal modulation. These effects, when strategically coupled with well-engineered materials and device architectures, enable compact and energy-efficient solutions that serve a growing demand for intelligence at the edge.

Through this review, we have highlighted the wide-ranging application domains empowered by these effects—from tactile sensors, accelerometers, and RF resonators to energy harvesters, memory devices, neuromorphic arrays, and optical modulators. Each application leverages a specific set of material and structural requirements, making material selection a key determinant of device performance and scalability. The comparative framework provided here aims to serve as a practical reference for aligning material properties with functional needs, particularly in CMOS-compatible processes.

Looking forward, the integration of these device functionalities into larger application ecosystems—such as AIoT, wearable health monitoring, immersive AR/VR, and soft robotics—will hinge on system-level co-design. This includes not only optimizing individual components, but also developing seamless signal flow across sensing, memory, and computing layers. Advances in heterogeneous integration, flexible substrates, and in-memory computing architectures are expected to further blur the boundaries between physical sensing and information processing, moving toward intelligent microsystems that are autonomous, adaptive, and deeply embedded in real-world environments.

Author contributions

Mengyao Xiao: conceptualization, investigation, writing original draft, and visualization. Aolei Xu: methodology, writing review and editing. Zhouli Sui: data curation, writing review and editing. Wenjie Zhang: supervision, and project administration. Huajun Liu: supervision and editing. Chengkuo Lee: conceptualization, supervision, funding acquisition, and writing review and editing.

Conflicts of interest

There are no conflicts to declare.

Data availability

Data sharing is not applicable to this article as no datasets were generated or analysed during the current study.

Acknowledgements

Authors acknowledges the funding support from the National Research Foundation Competitive Research Program (NRF-CRP28-2022-0002), RIE2025 MTC Individual Research Grant (M22K2c0084), RIE2025 Industry Alignment Fund – Industry Collaboration Projects (IAF-ICP I2301E0027), NUS Robotics Seed Grant Programme Projects (A-8003283-00-00), NUS Robotics Seed Grant Programme Projects (A-8003281-00-00) and NUS Microelectronics Seed Grant Programme Projects (A-8003551-00-00).

References

1 D. Li, H. Zhou, Z. Ren and C. Lee, *Small Sci.*, 2025, **5**, 2400250.
2 J. Zhu, X. Liu, Q. Shi, T. He, Z. Sun, X. Guo, W. Liu, O. B. Sulaiman, B. Dong and C. Lee, *Micromachines*, 2020, **11**, 7.
3 M. S. Yazici, B. Dong, D. Hasan, F. Sun and C. Lee, *Opt. Express*, 2020, **28**, 11524–11537.
4 B. Kawa, K. Śliwa, V. Ch Lee, Q. Shi and R. Walczak, *Energies*, 2020, **13**, 2800.
5 Y. Chang, J. Wei and C. Lee, *Nanophotonics*, 2020, **9**, 3049–3070.
6 Q. Qiao, M. S. Yazici, B. Dong, X. Liu, C. Lee and G. Zhou, *Opt. Lett.*, 2020, **45**, 5620–5623.
7 A. Luo, Y. Zhang, X. Guo, Y. Lu, C. Lee and F. Wang, *J. Microelectromech. Syst.*, 2021, **30**, 299–308.
8 Q. Qiao, H. Sun, X. Liu, B. Dong, J. Xia, C. Lee and G. Zhou, *Micromachines*, 2021, **12**, 1311.
9 B. Kawa, C. Lee and R. Walczak, *Energies*, 2022, **15**, 4468.
10 X. Le, Q. Shi, Z. Sun, J. Xie and C. Lee, *Adv. Sci.*, 2022, **9**, 2201056.
11 Q. Qiao, X. Liu, Z. Ren, B. Dong, J. Xia, H. Sun, C. Lee and G. Zhou, *ACS Photonics*, 2022, **9**, 2367–2377.
12 H. Sun, Q. Qiao, C. Lee and G. Zhou, *Phot. Nano. Fund. Appl.*, 2024, **58**, 101231.
13 H. Chen, H. Zhang, J. Zhou, C. Ma, Q. Huang, H. Wang, Q. Ren, N. Wang, C. Lee and Y. Ma, *Photon. Res.*, 2024, **12**, 1730–1740.
14 H. Sun, Q. Qiao, C. Lee and G. Zhou, *Laser Photonics Rev.*, 2025, **19**, 2400641.
15 J. Zhou, H. Zhang, Q. Qiao, H. Chen, Q. Huang, H. Wang, Q. Ren, N. Wang, Y. Ma and C. Lee, *Nat. Commun.*, 2024, **15**, 10260.
16 S. J. Z. Wong, K. Roy, C. Lee and Y. Zhu, *IEEE Trans. Ultrason. Eng.*, 2024, **71**, 622–637.
17 H. Liu, C. Lee, T. Kobayashi, C. J. Tay and C. Quan, *Sens. Actuators, A*, 2012, **186**, 242–248.

18 H. Liu, S. Zhang, T. Kobayashi, T. Chen and C. Lee, *Micro Nano Lett.*, 2014, **9**, 286–289.
19 T. Wang, T. Kobayashi and C. Lee, *Appl. Phys. Lett.*, 2015, **106**, 13501.
20 T. Wang, R. Sawada and C. Lee, *IEEE Electron Device Lett.*, 2015, **36**, 957–959.
21 T. Wang and C. Lee, *J. Microelectromech. Syst.*, 2015, **24**, 2083–2091.
22 Q. Shi, T. Wang and C. Lee, *Sci. Rep.*, 2016, **6**, 24946.
23 Q. Shi, T. Wang, T. Kobayashi and C. Lee, *Appl. Phys. Lett.*, 2016, **108**, 193902.
24 T. Wang, T. Kobayashi, B. Yang, H. Wang and C. Lee, *2016 IEEE 11th Annual International Conference on Nano/Micro Engineered and Molecular Systems (NEMS)*, 2016, pp. 294–299.
25 C. Sun, Q. Shi, M. S. Yazici, C. Lee and Y. Liu, *Sensors*, 2018, **18**, 4352.
26 H. Liu, J. Zhong, C. Lee, S.-W. Lee and L. Lin, *Appl. Phys. Rev.*, 2018, **5**, 41306.
27 C. Sun, Q. Shi, M. S. Yazici, T. Kobayashi, Y. Liu and C. Lee, *IEEE Sens. J.*, 2019, **19**, 860–867.
28 C. Sun, Q. Shi, D. Hasan, M. S. Yazici, M. Zhu, Y. Ma, B. Dong, Y. Liu and C. Lee, *Nano Energy*, 2019, **58**, 612–623.
29 M. Zhu, Q. Shi, T. He, Z. Yi, Y. Ma, B. Yang, T. Chen and C. Lee, *ACS Nano*, 2019, **13**, 1940–1952.
30 G. Tang, Z. Wang, X. Hu, S. Wu, B. Xu, Z. Li, X. Yan, F. Xu, D. Yuan, P. Li, Q. Shi and C. Lee, *Nanomaterials*, 2022, **12**, 1168.
31 L. Liu, Q. Shi, X. Guo, Z. Zhang and C. Lee, *EcoMat*, 2023, **5**, e12279.
32 M. Huang, M. Zhu, X. Feng, Z. Zhang, T. Tang, X. Guo, T. Chen, H. Liu, L. Sun and C. Lee, *ACS Nano*, 2023, **17**, 6435–6451.
33 C. Wang, Y. Hu, Y. Liu, Y. Shan, X. Qu, J. Xue, T. He, S. Cheng, H. Zhou, W. Liu, Z. H. Guo, W. Hua, Z. Liu, Z. Li and C. Lee, *Adv. Funct. Mater.*, 2023, **33**, 2303696.
34 Q. Huang, C. Ma, N. Wang, H. Zhang, C. Lee and Y. Ma, *Mater. Sci. Eng., R*, 2025, **164**, 100986.
35 R. Wang, H. Ye, X. Xu, J. Wang, R. Feng, T. Wang, B. Sheng, F. Liu, B. Shen, P. Wang and X. Wang, *Adv. Mater.*, 2025, **37**, 2414805.
36 W. Kho, H. Hwang, T. Noh, H. Kim, J. M. Lee and S.-E. Ahn, *Adv. Intell. Syst.*, 2024, **6**, 2400211.
37 Y. Chen, S. Wang, F. Liu, B. Wu, Y. Deng, R. Tao, Y. Wu and D. Gao, *J. Alloys Compd.*, 2025, **1010**, 178077.
38 J. Chen, J. Xu, J. Gu, B. Chen, H. Zhang, H. Qian, H. Liu, R. Shen, G. Lin, X. Yu, M. Zhang, Y. Ding, Y. Liu, J. Tang, H. Wu, C. Jin and G. Han, *Nat. Commun.*, 2025, **16**, 565.
39 E. Lim, Y. Park, C. Youn and S. Kim, *Nano Lett.*, 2025, **25**, 2166–2172.
40 H. Xu, F. Sun, E. Li, W. Guo, L. Hua, R. Wang, W. Li, J. Chu, W. Liu, J. Luo and Z. Sun, *Adv. Mater.*, 2025, **37**, 2414339.
41 S. Song, K.-H. Kim, R. Keneipp, M. Jung, N. Trainor, C. Chen, J. Zheng, J. M. Redwing, J. Kang, M. Drndić, R. H. Olsson III and D. Jariwala, *ACS Nano*, 2025, **19**, 8985–8996.
42 J. Bi, M. Faizan, X. Liu, Y. Ma, X. Wang and V. Stempitsky, *Chip*, 2025, **4**, 100129.
43 X. Yuan, X. Gao, X. Shen, J. Yang, Z. Li and S. Dong, *Nano Energy*, 2021, **85**, 105985.
44 U. Pierre Claver and G. Zhao, *Adv. Eng. Mater.*, 2021, **23**, 1–17.
45 J. P. George, P. F. Smet, J. Botterman, V. Bliznuk, W. Woestenborghs, D. Van Thourhout, K. Neyts and J. Beeckman, *ACS Appl. Mater. Interfaces*, 2015, **7**, 13350–13359.
46 R. M. R. Pinto, V. Gund, R. A. Dias, K. K. Nagaraja and K. B. Vinayakumar, *J. Microelectromech. Syst.*, 2022, **31**, 500–523.
47 Y. Birjis, S. Swaminathan, H. Nazemi, G. C. A. Raj, P. Munirathinam, A. Abu-Libdeh and A. Emadi, *Sensor*, 2022, **22**, 9151.
48 I. Ansari, J. P. George, G. F. Feutmba, T. Van De Veire, A. Pandey, J. Beeckman and D. Van Thourhout, *ACS Photonics*, 2022, **9**, 1944–1953.
49 K. Morimoto, I. Kanno, K. Wasa and H. Kotera, *Sens. Actuators, A*, 2010, **163**, 428–432.
50 C. Lee, T. Itoh and T. Suga, *Self-excited piezoelectric PZT microcantilevers for dynamic SFM-with inherent sensing and actuating capabilities*, 1999, vol. 72.
51 Y. B. Jeon, R. Sood, J. H. Jeong and S. G. Kim, *Sens. Actuators, A*, 2005, **122**, 16–22.
52 J. F. Tressler, S. Alkoy and R. E. Newnham, *J. Electroceram.*, 1998, **2**, 257–272.
53 F. Lu, H. P. Lee and S. P. Lim, *Smart Mater. Struct.*, 2004, **13**, 57–63.
54 L. Persano, A. Camposeo, F. Matino, R. Wang, T. Natarajan, Q. Li, M. Pan, Y. Su, S. Kar-Narayan, F. Auricchio, G. Scalet, C. Bowen, X. Wang and D. Pisignano, *Adv. Mater.*, 2024, **36**, 2405363.
55 C. Xiong, W. H. P. Pernice, J. H. Ngai, J. W. Reiner, D. Kumah, F. J. Walker, C. H. Ahn and H. X. Tang, *Nano Lett.*, 2014, **14**, 1419–1425.
56 M. Zgonik, P. Bernasconi, M. Duelli, R. Schlesser, P. Günter, M. H. Garrett, D. Rytz, Y. Zhu and X. Wu, *Phys. Rev. B: Condens. Matter Mater. Phys.*, 1994, **50**, 5941–5949.
57 M. N. Pionteck, M. Roeper, B. Koppitz, S. D. Seddon, M. Rüsing, L. Padberg, C. Eigner, C. Silberhorn, S. Sanna and L. M. Eng, *Phys. Rev. B*, 2025, **111**, 64109.
58 T. Mikolajick, S. Slesazeck, H. Mulaosmanovic, M. H. Park, S. Fichtner, P. D. Lomenzo, M. Hoffmann and U. Schroeder, *J. Appl. Phys.*, 2021, **129**, 100901.
59 Z. Kighelman, D. Damjanovic, M. Cantoni and N. Setter, *J. Appl. Phys.*, 2002, **91**, 1495–1501.
60 L. M. Sanchez, D. M. Potrepka, G. R. Fox, I. Takeuchi, K. Wang, L. A. Bendersky and R. G. Polcawich, *J. Mater. Res.*, 2013, **28**, 1920–1931.
61 D. Zhu, L. Shao, M. Yu, R. Cheng, B. Desiatov, C. J. Xin, Y. Hu, J. Holzgrafe, S. Ghosh, A. Shams-Ansari, E. Puma, N. Sinclair, C. Reimer, M. Zhang and M. Lončar, *Adv. Opt. Photonics*, 2021, **13**, 242.
62 G. Wingqvist, F. Tasnádi, A. Zukauskaite, J. Birch, H. Arwin and L. Hultman, *Appl. Phys. Lett.*, 2010, **97**, 112902.
63 X. Liu, A. W. Bruch and H. X. Tang, *Adv. Opt. Photonics*, 2023, **15**, 236.

64 F. Bernardini, V. Fiorentini and D. Vanderbilt, *Spontaneous polarization and piezoelectric constants of III-V nitrides*, 1997.
65 M. A. Fraga, H. Furlan, R. S. Pessoa and M. Massi, *Microsyst. Technol.*, 2014, **20**, 9–21.
66 H. Tian, J. Liu, A. Attanasio, A. Siddharth, T. Blesin, R. N. Wang, A. Voloshin, G. Lihachev, J. Riemensberger, S. Kenning, Y. Tian, T.-H. Chang, A. Bancora, V. Snigirev, V. Shadymov, T. Kippenberg and S. Bhave, *Adv. Opt. Photonics*, 2024, **16**, 749–867.
67 M. Pirro, B. Herrera, M. Assylbekova, G. Giribaldi, L. Colombo and M. Rinaldi, *Proceedings of the IEEE International Conference on Micro Electro Mechanical Systems (MEMS)*, Institute of Electrical and Electronics Engineers Inc., 2021, vol. 2021-Janua, pp. 646–649.
68 O. Ambacher, B. Christian, N. Feil, D. F. Urban, C. Elsässer, M. Prescher and L. Kirste, *J. Appl. Phys.*, 2021, **130**, 045102.
69 D. P. Yang, X. G. Tang, Q. J. Sun, J. Y. Chen, Y. P. Jiang, D. Zhang and H. F. Dong, *Mater. Horiz.*, 2024, **11**, 2802–2819.
70 Y. Lu, M. Reusch, N. Kurz, A. Ding, T. Christoph, M. Prescher, L. Kirste, O. Ambacher and A. Žukauskaitė, *APL Mater.*, 2018, **6**, 076105.
71 S. Barth, H. Bartzsch, D. Gloess, P. Frach, T. Herzog, S. Walter and H. Heuer, *IEEE Trans. Ultrason. Eng.*, 2014, **61**, 1329–1334.
72 W. Wang, M. Shen, C.-L. Zou, W. Fu, Z. Shen and H. X. Tang, *J. Appl. Phys.*, 2020, **128**, 184503.
73 M. Moustafa, Z. A. Waar and S. Yasin, *Institute of Electrical and Electronics Engineers (IEEE)*, 2024, pp. 1–6.
74 P. Kabakov, T. Kim, Z. Cheng, X. Jiang and S. Zhang, Annual Review of Materials Research Downloaded from **https://www.annualreviews.org**. Guest guest, 2025, 00, 25.
75 N. Ahbab, S. Naz, T. B. Xu and S. Zhang, *Micromachines*, 2025, **16**, 386.
76 Z. Pi, J. Zhang, C. Wen, Z. Bin Zhang and D. Wu, *Nano Energy*, 2014, **7**, 33–41.
77 B. Mohammadi, A. A. Yousefi and S. M. Bellah, *Polym. Test.*, 2007, **26**, 42–50.
78 L. Lu, W. Ding, J. Liu and B. Yang, *Nano Energy*, 2020, **78**, 105251.
79 F. C. Sun, A. M. Dongare, A. D. Asandei, S. Pamir Alpay and S. Nakhmanson, *J. Mater. Chem. C*, 2015, **3**, 8389–8396.
80 G. Rui, Y. Huang, X. Chen, R. Li, D. Wang, T. Miyoshi and L. Zhu, *J. Mater. Chem. C*, 2021, **9**, 894–907.
81 H. Zhu, Y. Wang, J. Xiao, M. Liu, S. Xiong, Z. J. Wong, Z. Ye, Y. Ye, X. Yin and X. Zhang, *Nat. Nanotechnol.*, 2015, **10**, 151–155.
82 W. Wu, L. Wang, Y. Li, F. Zhang, L. Lin, S. Niu, D. Chenet, X. Zhang, Y. Hao, T. F. Heinz, J. Hone and Z. L. Wang, *Nature*, 2014, **514**, 470–474.
83 W. Yue and J. Yi-Jian, *Optical Materials*, Elsevier, 2003, vol. 23, pp. 403–408.
84 Y. Wen, H. Chen, Z. Wu, W. Li and Y. Zhang, *APL Mater.*, 2024, **12**, 020601.
85 M. Zgonik, P. Bernasconi, M. Duelli, R. Schlesser, P. Günter, M. H. Garrett, D. Rytz, Y. Zhu and X. Wu, *Phys. Rev. B: Condens. Matter Mater. Phys.*, 1994, **50**, 5941–5949.
86 S. C. Abrahams, E. Buehler, W. C. Hamilton and S. J. Laplaca, *J. Phys. Chem. Solids*, 1973, **34**, 521–532.
87 H. Iwasaki, N. Uchida and T. Yamada, *Jpn. J. Appl. Phys., Part 1*, 1967, **6**, 1336.
88 J. I. Kushibiki, I. Takanaga and S. Nishiyama, *IEEE Trans. Ultrason. Eng.*, 2002, **49**, 125–135.
89 D. Lehninger, F. Müller, Y. Raffel, S. Yang, M. Neuber, S. Abdulazhanov, T. Kämpfe, K. Seidel and M. Lederer, *Adv. Electron. Mater.*, 2025, **11**, 2400686.
90 S. Starschich, T. Schenk, U. Schroeder and U. Boettger, *Appl. Phys. Lett.*, 2017, **110**, 182905.
91 B. Zeng, S. Xie, S. Zhang, H. Huang, C. Ju, S. Zheng, Q. Peng, Q. Yang, Y. Zhou and M. Liao, *Acta Mater.*, 2024, **272**, 119920.
92 I. Stolichnov, M. Cavalieri, E. Colla, T. Schenk, T. Mittmann, T. Mikolajick, U. Schroeder and A. M. Ionescu, *ACS Appl. Mater. Interfaces*, 2018, **10**, 30514–30521.
93 M. Hirose, T. Suzuki, H. Oka, K. Itakura, Y. Miyauchi and T. Tsukada, *Jpn. J. Appl. Phys., Part 1*, 1999, **38**, 5561–5563.
94 I. Coondoo, S. K. Agarwal and A. K. Jha, *Mater. Res. Bull.*, 2009, **44**, 1288–1292.
95 B. Y. Kim, I. T. Seo, Y. S. Lee, J. S. Kim, S. Nahm, C. Y. Kang, S. J. Yoon, J. H. Paik and Y. H. Jeong, *J. Am. Ceram. Soc.*, 2015, **98**, 119–124.
96 R. Pinho, R. Vilarinho, J. A. Moreira, F. Zorro, P. Ferreira, M. Ivanov, A. Tkach, M. E. Costa and P. M. Vilarinho, *J. Mater. Chem. C*, 2023, **11**, 7758–7771.
97 P. Li, J. Zhai, B. Shen, S. Zhang, X. Li, F. Zhu and X. Zhang, *Adv. Mater.*, 2018, **30**, 1–9.
98 H. Liu, H. Wu, K. P. Ong, T. Yang, P. Yang, P. K. Das, X. Chi, Y. Zhang, C. Diao, W. K. A. Wong, E. P. Chew, Y. F. Chen, C. K. I. Tan, A. Rusydi, M. B. H. Breese, D. J. Singh, L. Q. Chen, S. J. Pennycook and K. Yao, *Science*, 2020, **369**, 292–297.
99 B. Lin, K. P. Ong, T. Yang, Q. Zeng, H. K. Hui, Z. Ye, C. Sim, Z. Yen, P. Yang, Y. Dou, X. Li, X. Gao, C. K. I. Tan, Z. S. Lim, S. Zeng, T. Luo, J. Xu, X. Tong, P. W. F. Li, M. Ren, K. Zeng, C. Sun, S. Ramakrishna, M. B. H. Breese, C. Boothroyd, C. Lee, D. J. Singh, Y. M. Lam and H. Liu, *Nature*, 2024, **633**, 798–803.
100 J. U. Woo, I. S. Kim, B. Kim and S. Nahm, *Appl. Surf. Sci.*, 2022, **593**, 153464.
101 W. Othman, Z. H. A. Lai, C. Abril, J. S. Barajas-Gamboa, R. Corcelles, M. Kroh and M. A. Qasaimeh, *Front. Robot. AI*, 2022, **8**, 1–43.
102 Y. Tian, P. He, B. Yang, Z. Yi, L. Lu and J. Liu, *IEEE Sens. J.*, 2020, **20**, 8463–8468.
103 H. Wei, W. Geng, K. Bi, T. Li, X. Li, X. Qiao, Y. Shi, H. Zhang, C. Zhao, G. Xue and X. Chou, *Micromachines*, 2022, **13**, 1–14.
104 X. Gong, Y.-C. Kuo, G. Zhou, W.-J. Wu and W.-H. Liao, *Microsyst. Nanoeng.*, 2023, **9**, 23.
105 Y. Wang, H. Ding, X. Le, W. Wang and J. Xie, *Sens. Actuators, A*, 2017, **254**, 126–133.
106 C. Ge and E. Cretu, *Microsyst. Nanoeng.*, 2023, **9**, 151.
107 M. Schlögl, S. Köpl, J. Hiesberger, M. Schneider and U. Schmid, *Sens. Actuators, A*, 2022, **346**, 113829.

108 M. T. Chorsi, E. J. Curry, H. T. Chorsi, R. Das, J. Baroody, P. K. Purohit, H. Ilies and T. D. Nguyen, *Adv. Mater.*, 2019, **31**, 1–15.
109 J. Zhou, Y. Gu, P. Fei, W. Mai, Y. Gao, R. Yang, G. Bao and Z. L. Wang, *Nano Lett.*, 2008, **8**, 3035–3040.
110 P. Joshi, S. Kumar, V. K. Jain, J. Akhtar and J. Singh, *J. Microelectromech. Syst.*, 2019, **28**, 382–389.
111 J. Lee, W. Choi, Y. K. Yoo, K. S. Hwang, S. M. Lee, S. Kang, J. Kim and J. H. Lee, *Sensors*, 2014, **14**, 22199–22207.
112 M. Schlögl, J. Weißenbach, M. Schneider and U. Schmid, *Sens. Actuators, A*, 2023, **349**, 114067.
113 M. Olfatnia, T. Xu, J. M. Miao, L. S. Ong, X. M. Jing and L. Norford, *Sens. Actuators, A*, 2010, **163**, 32–36.
114 W. Lin, B. Wang, G. Peng, Y. Shan, H. Hu and Z. Yang, *Adv. Sci.*, 2021, **8**(8), 2002817.
115 H. Oh, G. C. Yi, M. Yip and S. A. Dayeh, *Sci. Adv.*, 2020, **6**, 1–14.
116 M. Liu, Z. Dai, Y. Zhao, H. Ling, L. Sun, C. Lee, M. Zhu and T. Chen, *ACS Appl. Mater. Interfaces*, 2024, **16**, 53207–53219.
117 S. Chun, J. S. Kim, Y. Yoo, Y. Choi, S. J. Jung, D. Jang, G. Lee, K. Il Song, K. S. Nam, I. Youn, D. Son, C. Pang, Y. Jeong, H. Jung, Y. J. Kim, B. D. Choi, J. Kim, S. P. Kim, W. Park and S. Park, *Nat. Electron.*, 2021, **4**, 429–438.
118 J. Zhang, H. Yao, J. Mo, S. Chen, Y. Xie, S. Ma, R. Chen, T. Luo, W. Ling, L. Qin, Z. Wang and W. Zhou, *Nat. Commun.*, 2022, **13**, 1–9.
119 Y. Wang, M. Zhu, X. Wei, J. Yu, Z. Li and B. Ding, *Chem. Eng. J.*, 2021, **425**, 130599.
120 L. Li, S. Zhao, W. Ran, Z. Li, Y. Yan, B. Zhong, Z. Lou, L. Wang and G. Shen, *Nat. Commun.*, 2022, **13**, 5975.
121 B. Paschke, A. Wixforth, D. Denysenko and D. Volkmer, *ACS Sens.*, 2017, **2**, 740–747.
122 L. Zhou, Z. Hu, P. Wang, N. Gao, B. Zhai, M. Ouyang, G. Zhang, B. Chen, J. Luo, S. Jiang, H. Y. Li and H. Liu, *Sens. Actuators, B*, 2022, **361**, 131735.
123 X. Lu, Y. Yuan, F. Chen, X. Hou, Y. Guo, L. Reindl, Y. Fu, W. Luo and D. Zhao, *Microsyst. Nanoeng.*, 2025, **11**, 44.
124 S. Xiong, J. Zhou, J. Wu, H. Li, W. Zhao, C. He, Y. Liu, Y. Chen, Y. Fu and H. Duan, *ACS Appl. Mater. Interfaces*, 2021, **13**, 42094–42103.
125 Y. Liu, J. Zhou, S. Wen, Y. Chen, Y. Q. Fu and H. Duan, *Sens. Actuators, B*, 2023, **393**, 134289.
126 B. Cui, X. Lang, Z. Ren, L. Cheng, D. Yang and W. Wang, *Sens. Actuators, B*, 2025, **423**, 136817.
127 K. Roy, D. Sim, L. Wang, Z. Zhang, X. Guo, Y. Zhu, S. Swarup and C. Lee, *Adv. Sci.*, 2025, **12**, e04954.
128 W. Lu, J. Fu, N. Wu and Y. He, *Renewable Sustainable Energy Rev.*, 2025, **214**, 115521.
129 L. Wang, T. He, Z. Zhang, L. Zhao, C. Lee, G. Luo, Q. Mao, P. Yang, Q. Lin, X. Li, R. Maeda and Z. Jiang, *Nano Energy*, 2021, **80**, 105555.
130 M. Safaei, H. A. Sodano and S. R. Anton, *Smart Mater. Struct.*, 2019, **28**, 113001.
131 R. Bhatnagar, V. Yadav, U. Kumar and M. F. Carrasco, *Energy Technol.*, 2025, **13**, 2401455.
132 H. Liu, C. Lee, T. Kobayashi, C. J. Tay and C. Quan, *Smart Mater. Struct.*, 2012, **21**, 035005.
133 K. B. Kim, J. Y. Cho, J. Hamid, J. H. Ahn, S. Do Hong, S. B. Woo and T. H. Sung, *Energy Convers. Manage.*, 2018, **171**, 31–37.
134 K. Mou, X. Ji, J. Liu, H. Zhou, H. Tian, X. Li and H. Liu, *J. Traffic Transp. Eng., Engl. Ed.*, 2025, **12**(1), 68–86.
135 H. Liu, C. J. Tay, C. Quan, T. Kobayashi and C. Lee, *Microsyst. Technol.*, 2011, **17**, 1747–1754.
136 P. Chaudhary and P. Azad, *J. Electron. Mater.*, 2020, **49**, 6455–6464.
137 M. A. Mangi, H. Elahi, A. Ali, H. Jabbar, A. Bin Aqeel, A. Farrukh, S. Bibi, W. A. Altabey, S. A. Kouritem and M. Noori, *Sens. Actuators Rep.*, 2025, **9**, 100302.
138 Y. Goh, J. Hwang, M. Kim, Y. Lee, M. Jung and S. Jeon, *ACS Appl. Mater. Interfaces*, 2021, **13**, 59422–59430.
139 P. Gao, M. Duan, G. Yang, W. Zhang and C. Jia, *Nano Lett.*, 2024, **24**, 10767–10775.
140 J. Fang, Z. Tang, X. C. Lai, F. Qiu, Y. P. Jiang, Q. X. Liu, X. G. Tang, Q. J. Sun, Y. C. Zhou, J. M. Fan and J. Gao, *ACS Appl. Mater. Interfaces*, 2024, **16**, 31348–31362.
141 M. Lanza, A. Sebastian, W. D. Lu, M. Le Gallo, M. F. Chang, D. Akinwande, F. M. Puglisi, H. N. Alshareef, M. Liu and J. B. Roldan, *Science*, 2022, **376**, eabj9979.
142 M. Zhang, Q. Qin, X. Chen, R. Tang, A. Han, S. Yao, R. Dan, Q. Wang, Y. Wang, H. Gu, H. Zhang, E. Hu, L. Wang, J. Xu and Y. Tong, *Ceram. Int.*, 2022, **48**, 16263–16272.
143 W. Kho, H. Hwang and S. E. Ahn, *Adv. Electron. Mater.*, 2024, **10**, 1–9.
144 F. Risch, A. Gilani, S. Kamaei, A. M. Ionescu and I. Stolichnov, *Appl. Phys. Lett.*, 2024, **125**, 152902.
145 V. Garcia and M. Bibes, *Nat. Commun.*, 2014, **5**, 4289.
146 H. Wang, Y. Ma, Q. Zheng, K. Cao, Y. Lu and H. Xie, *Micromachines*, 2021, **12**, 1257.
147 H. H. Cheng and W. Fang, *Sens. Actuators, A*, 2024, **377**, 115717.
148 W. T. Shih, W. H. Tsou, D. Vasic, F. Costa and W. J. Wu, *Micromachines*, 2025, **16**, 1–17.
149 C. Gazzola, V. Zega, F. Cerini, S. Adorno and A. Corigliano, *J. Microelectromech. Syst.*, 2023, **32**, 626–637.
150 A. Kumar, A. Varghese, A. Sharma, M. Prasad, V. Janyani, R. P. Yadav and K. Elgaid, *Sens. Actuators, A*, 2022, **347**, 113887.
151 G. Boztas, *Neural Comput. Appl.*, 2023, **35**, 6801–6811.
152 A. Rahaman and B. Kim, *Sci. Rep.*, 2020, **10**, 1–10.
153 F. M. Mayor, S. Malik, A. G. Primo, S. Gyger, W. Jiang, T. P. M. Alegre and A. H. Safavi-Naeini, *Nat. Commun.*, 2025, **16**, 2576.
154 K. Airola, S. Mertin, J. Likonen, E. Hartikainen, K. Mizohata, J. Dekker, A. Thanniyil Sebastian and T. Pensala, *Materialia*, 2022, **22**, 101403.
155 M. Eichenfield, J. Chan, R. M. Camacho, K. J. Vahala and O. Painter, *Nature*, 2009, **462**, 78–82.
156 T. Blésin, W. Kao, A. Siddharth, R. N. Wang, A. Attanasio, H. Tian, S. A. Bhave and T. J. Kippenberg, *Nat. Commun.*, 2024, **15**, 6096.
157 M. Oshio, S. Kanna and K. Iizawa, *Jpn. J. Appl. Phys., Part 1*, 2006, **45**, 4671–4674.

158 A. Khurana, P. Jiang and K. C. Balram, *Phys. Rev. Appl.*, 2022, **18**(5), 054030.
159 J. Xie, M. Shen, Y. Xu, W. Fu, L. Yang and H. X. Tang, *Nat. Electron.*, 2023, **6**, 301–306.
160 H. Tian, J. Liu, B. Dong, J. C. Skehan, M. Zervas, T. J. Kippenberg and S. A. Bhave, *Nat. Commun.*, 2020, **11**, 3073.
161 S. Ghosh and G. Piazza, *APL Photonics*, 2016, **1**, 036101.
162 S. Meesala, S. Wood, D. Lake, P. Chiappina, C. Zhong, A. D. Beyer, M. D. Shaw, L. Jiang and O. Painter, *Nat. Phys.*, 2024, **20**, 871–877.
163 A. E. Hassanien, S. Link, Y. Yang, E. Chow, L. L. Goddard and S. Gong, *Photonics Res.*, 2021, **9**, 1182.
164 T. C. van Thiel, M. J. Weaver, F. Berto, P. Duivestein, M. Lemang, K. L. Schuurman, M. Žemlička, F. Hijazi, A. C. Bernasconi, C. Ferrer, E. Cataldo, E. Lachman, M. Field, Y. Mohan, F. K. de Vries, C. C. Bultink, J. C. van Oven, J. Y. Mutus, R. Stockill and S. Gröblacher, *Nat. Phys.*, 2025, **21**, 401–405.
165 S. Abel, F. Eltes, J. E. Ortmann, A. Messner, P. Castera, T. Wagner, D. Urbonas, A. Rosa, A. M. Gutierrez, D. Tulli, P. Ma, B. Baeuerle, A. Josten, W. Heni, D. Caimi, L. Czornomaz, A. A. Demkov, J. Leuthold, P. Sanchis and J. Fompeyrine, *Nat. Mater.*, 2019, **18**, 42–47.
166 L. Chen, C. Liu, M. Li, W. Song, W. Wang, Z. Wang, N. Wang and Y. Zhu, *ACS Appl. Electron. Mater.*, 2023, **5**, 612–622.
167 I. T. Chen, B. Li, S. Lee, S. Chakravarthi, K. M. Fu and M. Li, *Nat. Commun.*, 2023, **14**, 7594.
168 F. Eltes, G. E. Villarreal-Garcia, D. Caimi, H. Siegwart, A. A. Gentile, A. Hart, P. Stark, G. D. Marshall, M. G. Thompson, J. Barreto, J. Fompeyrine and S. Abel, *Nat. Mater.*, 2020, **19**, 1164–1168.
169 J. Shen, Y. Fan, Z. Xu, L. Wu, Y. Wang, X. Li, X. Gan, Y. Zhang and Y. Su, *Laser Photonics Rev.*, 2023, **17**, 2200248.
170 B. Kim, I. Seo, Y. Lee, J. Kim, S. Nahm, C. Kang, S. Yoon, J. Paik and Y. Jeong, *J. Am. Ceram. Soc.*, 2015, **98**, 119–124.
171 P. Lei, M. Xu, Y. Bai, Z. Chen and X. Xie, *Nat. Commun.*, 2024, **15**, 3877.
172 H. Shi, C. Huang, L. Yu, Q. Huang, M. Cheng and J. Sun, *J. Lightwave Technol.*, 2023, **41**, 6348–6355.
173 N. S. Yama, I.-T. Chen, S. Chakravarthi, B. Li, C. Pederson, B. E. Matthews, S. R. Spurgeon, D. E. Perea, M. G. Wirth, P. V. Sushko, M. Li and K.-M. C. Fu, *Adv. Mater.*, 2024, **36**, 2305434.
174 K. C. Balram and K. Srinivasan, *Adv. Quantum Technol.*, 2022, **5**, 2100095.
175 J. He and X. Sun, *Laser Photonics Rev.*, 2024, 2401525.
176 J. Zheng, X. Liu and Y. Yang, *IEEE Electron Device Lett.*, 2025, **46**, 167–170.
177 H. Zhou, D. Li, Q. Lv and C. Lee, *Chem. Soc. Rev.*, 2025, **54**, 5342–5432.
178 G. Yang, H. Wang, S. Mu, H. Xie, T. Wang, C. He, M. Shen, M. Liu, C. G. Van de Walle and H. X. Tang, *Nat. Commun.*, 2024, **15**, 1–10.
179 W. Liu, S. Xu and C. Lee, *Science*, 2025, **389**, 806–810.
180 J. Geler-Kremer, F. Eltes, P. Stark, D. Stark, D. Caimi, H. Siegwart, B. Jan Offrein, J. Fompeyrine and S. Abel, *Nat. Photonics*, 2022, **16**, 491–497.
181 M. He, M. Xu, Y. Ren, J. Jian, Z. Ruan, Y. Xu, S. Gao, S. Sun, X. Wen, L. Zhou, L. Liu, C. Guo, H. Chen, S. Yu, L. Liu and X. Cai, *Nat. Photonics*, 2019, **13**, 359–364.
182 R. T. Chen, R. L. Nelson, J. Luo, C.-J. Chung, A. K.-Y. Jen, X. Zhang, A. Hosseini, H. Subbaraman and C. Y.-C. Lee, *J. Light Technol.*, 2016, **34**, 2941–2951.
183 S. Abel, F. Eltes, J. E. Ortmann, A. Messner, P. Castera, T. Wagner, D. Urbonas, A. Rosa, A. M. Gutierrez, D. Tulli, P. Ma, B. Baeuerle, A. Josten, W. Heni, D. Caimi, L. Czornomaz, A. A. Demkov, J. Leuthold, P. Sanchis and J. Fompeyrine, *Nat. Mater.*, 2018, **18**, 42–47.
184 B. Chmielak, M. Waldow, C. Matheisen, C. Ripperda, J. Bolten, T. Wahlbrink, M. Nagel, F. Merget, H. Kurz, E. L. Wooten, K. M. Kissa, A. Yi-Yan, E. J. Murphy, D. A. Lafaw, P. F. Hallemeier, D. Maack, D. V. Attanasio, D. J. Fritz, G. J. McBrien, D. E. Bossi, R. A. Soref and J. P. Lorenzo, *Opt. Express*, 2011, **19**(18), 17212–17219.
185 M. Xu, M. He, H. Zhang, J. Jian, Y. Pan, X. Liu, L. Chen, X. Meng, H. Chen, Z. Li, X. Xiao, S. Yu, S. Yu and X. Cai, *Nat. Commun.*, 2020, **11**, 1–7.
186 L. Xu, S. Zhong, T. Yue, Z. Zhang, X. Lu, Y. Lin, L. Li, Y. Tian, T. Jin, Q. Zhang and C. Lee, *EcoMat*, 2024, **6**, e12448.
187 Z. Zhang, T. He, M. Zhu, Q. Shi and C. Lee, *2020 IEEE 33rd International Conference on Micro Electro Mechanical Systems (MEMS)*, 2020, pp. 80–83.
188 B. Dong, Q. Shi, Y. Yang, F. Wen, Z. Zhang and C. Lee, *Nano Energy*, 2021, **79**, 105414.
189 Z. Sun, M. Zhu, Z. Zhang, Z. Chen, Q. Shi, X. Shan, R. C. H. Yeow and C. Lee, *Adv. Sci.*, 2021, **8**, 2100230.
190 Q. Shi, Z. Zhang, Y. Yang, X. Shan, B. Salam and C. Lee, *ACS Nano*, 2021, **15**, 18312–18326.
191 T. Leng, L. Li and C. Lee, *AI Sens.*, 2025, **1**, 1.
192 H. Zhou, D. Li and C. Lee, *AI Sens.*, 2025, **1**, 5.
193 X. Guo, L. Wang, Z. Jin and C. Lee, *Nano-Micro Lett.*, 2024, **17**, 76.
194 Y. Pang, X. Zhu, T. He, S. Liu, Z. Zhang, Q. Lv, P. Yi and C. Lee, *Adv. Mater.*, 2024, **36**, 2404763.
195 F. Wen, C. Wang and C. Lee, *Nano Res.*, 2023, **16**, 11801–11821.
196 Y. Pang, X. Zhu, Y. Jin, Z. Yang, S. Liu, L. Shen, X. Li and C. Lee, *Appl. Energy*, 2023, **348**, 121515.
197 A. Luo, W. Xu, J. Sun, K. Xi, S. Tang, X. Guo, C. Lee and F. Wang, *Nano Energy*, 2023, **105**, 108030.
198 Y. Pang, X. Zhu, C. Lee and S. Liu, *Nano Energy*, 2022, **97**, 107219.
199 L. Liu, X. Guo, W. Liu and C. Lee, *Nanomaterials*, 2021, **11**, 2975.
200 Q. Zhang, Z. Zhang, Q. Liang, Q. Shi, M. Zhu and C. Lee, *Adv. Sci.*, 2021, **8**, 2004727.
201 C. Lee, Y. Qin and Y.-C. Wang, *MRS Bull.*, 2025, **50**, 428–438.
202 F. A. Hassani, W. Y. X. Peh, G. G. L. Gammad, R. P. Mogan, T. K. Ng, T. L. C. Kuo, L. G. Ng, P. Luu, S.-C. Yen and C. Lee, *Adv. Sci.*, 2017, **4**, 1700143.

203 F. A. Hassani, G. G. L. Gammad, R. P. Mogan, T. K. Ng, T. L. C. Kuo, L. G. Ng, P. Luu, N. V. Thakor, S.-C. Yen and C. Lee, *Adv. Mater. Technol.*, 2018, **3**, 1700184.
204 B. W. Soon, N. Singh, J. M. Tsai and C. Lee, *The 8th Annual IEEE International Conference on Nano/Micro Engineered and Molecular Systems*, 2013, pp. 562–565.
205 B. Soon, N. Singh, J. M. Tsai and C. Lee, *2013 Transducers & Eurosensors XXVII: The 17th International Conference on Solid-State Sensors, Actuators and Microsystems (TRANSDUCERS & EUROSENSORS XXVII)*, 2013, pp. 892–895.
206 W. Xiang and C. Lee, *Appl. Phys. Lett.*, 2010, **96**, 193113.
207 B. W. Soon, N. Singh, J. M. Tsai and C. Lee, *IEEE Nanotechnol. Magazine*, 2013, **7**, 24–28.
208 P. Singh, C. G. Li, P. Pitchappa and C. Lee, *IEEE Electron Device Lett.*, 2013, **34**, 987–989.
209 B. W. Soon, E. Jiaqiang Ng, Y. Qian, N. Singh, M. Julius Tsai and C. Lee, *Appl. Phys. Lett.*, 2013, **103**, 53122.
210 B. Soon, E. J. Ng, N. Singh, J. M. Tsai, Y. Qian and C. Le, *J. Microelectromech. Syst.*, 2013, **22**, 1004–1006.
211 C. Chen, Y. Zhou, L. Tong, Y. Pang and J. Xu, *Adv. Mater.*, 2025, **37**, 2400332.
212 I.-S. Kim, B. Kim, S.-J. Chae and S. Nahm, *Adv. Intell. Syst.*, 2024, **6**, 2300634.
213 R. Athle and M. Borg, *Adv. Intell. Syst.*, 2024, **6**, 1–9.
214 S. R. Greig, C. J. Firby, T. Muneshwar, S. Alagöz, E. Hopmann, B. N. Carnio, M. Zhang, G. Ciarniello, K. Cadien and A. Y. Elezzabi, *Sci. Adv.*, 2025, **11**, 1–8.
215 S. Wang, X. Chen, C. Zhao, Y. Kong, B. Lin, Y. Wu, Z. Bi, Z. Xuan, T. Li, Y. Li, W. Zhang, E. Ma, Z. Wang and W. Ma, *Nat. Electron.*, 2023, **6**, 281–291.
216 S. Yu, *Proc. IEEE*, 2018, **106**, 260–285.
217 X. Du, H. Sun, H. Wang, J. Li, Y. Yin and X. Li, *ACS Appl. Mater. Interfaces*, 2022, **14**, 1355–1361.
218 X. Yan, J. Sun, Y. Zhang, Z. Zhao, L. Wang, J. Niu, X. Jia, Z. Zhang, X. Han, Y. Shao and Z. Guo, *Mater. Today Nano*, 2023, **22**, 100343.
219 M. J. Sultan, A. Bag, S. J. Hong, G. Wang, S. Kumar, H. H. Chouhdry and N. E. Lee, *Nano Energy*, 2024, **131**, 110202.
220 Y. Lee, J. Y. Oh, W. Xu, O. Kim, T. R. Kim, J. Kang, Y. Kim, D. Son, J. B. H. Tok, M. J. Park, Z. Bao and T. W. Lee, *Sci. Adv.*, 2018, **4**, 1–9.
221 Y. Zhuge, Z. Ren, Z. Xiao, Z. Zhang, X. Liu, W. Liu, S. Xu, C. P. Ho, N. Li and C. Lee, *Adv. Sci.*, 2025, 2500525.
222 Z. Zhang, X. Liu, H. Zhou, S. Xu and C. Lee, *Small Struct.*, 2024, **5**, 2300325.
223 X. Liu, Z. Zhang, J. Zhou, W. Liu, G. Zhou and C. Lee, *ACS Nano*, 2024, **18**, 22938–22948.
224 Z. Xiao, Z. Ren, Y. Zhuge, Z. Zhang, J. Zhou, S. Xu, C. Xu, B. Dong and C. Lee, *Adv. Sci.*, 2024, **11**, 2408597.
225 Z. Ren, Z. Zhang, Y. Zhuge, Z. Xiao, S. Xu, J. Zhou and C. Lee, *Nano-Micro Lett.*, 2025, **17**, 261.
226 T. He, F. Wen, Y. Yang, X. Le, W. Liu and C. Lee, *Anal. Chem.*, 2023, **95**, 490–514.
227 Z. H. Guo, Z. Zhang, K. An, T. He, Z. Sun, X. Pu and C. Lee, *Research*, 2025, **6**, 154.
228 J. Chen, T. He, Z. Du and C. Lee, *Nano Energy*, 2023, **117**, 108898.
229 Q. Liang, D. Zhang, T. He, Z. Zhang, H. Wang, S. Chen and C. Lee, *ACS Nano*, 2024, **18**, 600–611.
230 Z. Sun, M. Zhu, Z. Zhang, Z. Chen, Q. Shi, X. Shan and C. Lee, *2021 IEEE 34th International Conference on Micro Electro Mechanical Systems (MEMS)*, 2021, pp. 591–594.
231 T. Chen, Q. Shi, M. Zhu, T. He, L. Sun, L. Yang and C. Lee, *ACS Nano*, 2018, **12**, 11561–11571.
232 T. Jin, Z. Sun, L. Li, Q. Zhang, M. Zhu, Z. Zhang, G. Yuan, T. Chen, Y. Tian, X. Hou and C. Lee, *Nat. Commun.*, 2020, **11**, 5381.
233 X. Hou, M. Zhu, L. Sun, T. Ding, Z. Huang, Y. Shi, Y. Su, L. Li, T. Chen and C. Lee, *Nano Energy*, 2022, **93**, 106894.
234 S. Duan, Q. Shi, J. Hong, D. Zhu, Y. Lin, Y. Li, W. Lei, C. Lee and J. Wu, *ACS Nano*, 2023, **17**, 1355–1371.
235 Q. Shi, Z. Sun, X. Le, J. Xie and C. Lee, *ACS Nano*, 2023, **17**, 4985–4998.
236 T. Wu, H. Deng, Z. Sun, X. Zhang, C. Lee and X. Zhang, *iScience*, 2023, **26**(8), 107249.
237 T. Wang, T. Jin, W. Lin, Y. Lin, H. Liu, T. Yue, Y. Tian, L. Li, Q. Zhang and C. Lee, *ACS Nano*, 2024, **18**, 9980–9996.
238 Y. Xu, Z. Sun, Z. Bai, H. Shen, R. Wen, F. Wang, G. Xu and C. Lee, *Nat. Commun.*, 2024, **15**, 6022.
239 X. Zhao, Z. Sun and C. Lee, *Adv. Funct. Mater.*, 2024, **34**, 2409558.
240 Y. Sun, T. Chen, D. Li, H. Li, T. Ji, F. Wang, L. Sun, C. Lee and H. Liu, *Adv. Mater.*, 2025, **2502203**, 1–16.
241 C. Lee, T. Itoh, R. Maeda and T. Suga, *Rev. Sci. Instrum.*, 1997, **68**, 2091–2100.
242 C. Lee, S. Kawano, T. Itoh and T. Suga, *J. Mater. Sci.*, 1996, **31**, 4559–4568.
243 C. Lee, T. Itoh, G. Sasaki and T. Suga, *Mater. Chem. Phys.*, 1996, **44**, 25–29.
244 C. Lee, T. Itoh and T. Suga, *IEEE Trans. Ultrason. Eng.*, 1996, **43**, 553–559.
245 C. Lee, T. Itoh, T. Ohashi, R. Maeda and T. Suga, *J. Vac. Sci. Technol., B:Nanotechnol. Microelectron.:Mater., Process., Meas., Phenom.*, 1997, **15**, 1559–1563.
246 A. Rampal and R. N. Kleiman, *Microsyst. Nanoeng.*, 2021, **7**, 29.
247 L. Chang, A. Boes, X. Guo, D. T. Spencer, M. J. Kennedy, J. D. Peters, N. Volet, J. Chiles, A. Kowligy, N. Nader, D. D. Hickstein, E. J. Stanton, S. A. Diddams, S. B. Papp and J. E. Bowers, *Laser Photonics Rev.*, 2018, **12**, 1800149.
248 R. Stockill, M. Forsch, F. Hijazi, G. Beaudoin, K. Pantzas, I. Sagnes, R. Braive and S. Gröblacher, *Nat. Commun.*, 2022, **13**, 6583.
249 C. M. Lueng, H. L. W. Chan, W. K. Fong, C. Surya and C. L. Choy, *Mater. Res. Soc. Symp. Proc.*, 1999, **572**, 389–394.
250 O. Bilgen, M. Amin Karami, D. J. Inman and M. I. Friswell, *Smart Mater. Struct.*, 2011, **20**, 055024.
251 R. Ramesh, *et al.*, *ChemInform*, 2003, **34**, 1719–1722.
252 H. Qi, A. Xie, A. Tian and R. Zuo, *Adv. Energy Mater.*, 2020, **10**, 1–8.
253 T. Kobayashi, S. Oyama, N. Makimoto, H. Okada, T. Itoh and R. Maeda, *Sens. Actuators, A*, 2013, **198**, 87–90.

254 A. Varghese, A. H. Pandey, P. Sharma, Y. Yin, N. V. Medhekar and S. Lodha, *Nano Lett.*, 2024, **24**, 8472–8480.
255 A. Kumar and R. Prajesh, *Sens. Actuators, A*, 2022, **339**, 113498.
256 X. Yan, H. Qu, Y. Chang, W. Pang and X. Duan, *Nanotechnol. Precis. Eng.*, 2022, **5**, 13005.
257 S. Song, D. Chen, H. Wang, Q. Guo, W. Wang, M. Wu and W. Yu, *Sens. Actuators, B*, 2018, **266**, 204–212.
258 X. Yan, H. Qu, Y. Chang, W. Pang, Y. Wang and X. Duan, *ACS Appl. Mater. Interfaces*, 2020, **12**, 10009–10017.
259 J. Hu, H. Qu, Y. Chang, W. Pang, Q. Zhang, J. Liu and X. Duan, *Sens. Actuators, B*, 2018, **274**, 419–426.
260 G. Zeng, C. Wu, Y. Chang, C. Zhou, B. Chen, M. Zhang, J. Li, X. Duan, Q. Yang and W. Pang, *ACS Sens.*, 2019, **4**, 1524–1533.
261 A. K. Johar, G. K. Sharma, T. B. Kumar, T. Varma, C. Periasamy, A. Agarwal and D. Boolchandani, *J. Electron. Mater.*, 2021, **50**, 5387–5395.
262 J. Liu, Z. Zhao, Z. Fang, Z. Liu, Y. Zhu and L. Du, *Sens. Actuators, B*, 2020, **308**, 127694.
263 Y. Chang, N. Tang, H. Qu, J. Liu, D. Zhang, H. Zhang, W. Pang and X. Duan, *Sci. Rep.*, 2016, **6**, 1–12.
264 H. Zhao, S. Fan, Y. Chen, Z. Feng, H. Zhang, W. Pang, D. Zhang and M. Zhang, *ACS Appl. Mater. Interfaces*, 2017, **9**, 40774–40781.
265 L. Wang, Y. Wang, M. Tietze, B. P. Madeira, R. P. Martins, P.-I. Mak, N. Chanut, D. Rajagopal, M. Sugihara, R. Ameloot and C. Wang, *Microsyst. Nanoeng.*, 2025, **11**, 69.
266 Y. Q. Hu, W. Xu, N. T. Liu, Y. K. Li, X. Deng, Z. Guan, Y. F. Zheng, S. Yang, R. Huang, F. Y. Yue, Y. Y. Zhang, H. Peng, B. Bin Chen, N. Zhong, P. H. Xiang and C. G. Duan, *Adv. Opt. Mater.*, 2024, **12**, 2302887.
267 Z. Xia, X. Sun, Z. Wang, J. Meng, B. Jin and T. Wang, *Nano-Micro Lett.*, 2025, **17**, 217.
268 S. Song, K.-H. Kim, R. Keneipp, M. Jung, N. Trainor, C. Chen, J. Zheng, J. M. Redwing, J. Kang, M. Drndić, R. H. Olsson III and D. Jariwala, *ACS Nano*, 2025, **19**, 8985–8996.
269 W. Di Zhang, Z. Z. Song, S. Q. Tang, J. C. Wei, Y. Cheng, B. Li, S. Y. Chen, Z. Bin Chen and A. Q. Jiang, *Nat. Commun.*, 2025, **16**, 1–10.
270 M. Lee, Y. C. Jung, J.-H. Kim, D. M. Narayan, S. Kang, W. Y. Park, K. Im and J. Kim, *Nano Convergence*, 2025, **12**, 15.
271 Y. Chen, S. Wang, F. Liu, B. Wu, Y. Deng, R. Tao, Y. Wu and D. Gao, *J. Alloys Compd.*, 2025, **1010**, 178077.
272 V. Garcia and M. Bibes, *Nat. Commun.*, 2014, **5**, 4289.
273 Z. Wen and D. Wu, *Adv. Mater.*, 2020, **32**, 1–19.
274 B. B. Tian, J. L. Wang, S. Fusil, Y. Liu, X. L. Zhao, S. Sun, H. Shen, T. Lin, J. L. Sun, C. G. Duan, M. Bibes, A. Barthélémy, B. Dkhil, V. Garcia, X. J. Meng and J. H. Chu, *Nat. Commun.*, 2016, **7**, 1–6.
275 D. J. Kim, H. Lu, S. Ryu, C. W. Bark, C. B. Eom, E. Y. Tsymbal and A. Gruverman, *Nano Lett.*, 2012, **12**, 5697–5702.
276 C. Ma, Z. Luo, W. Huang, L. Zhao, Q. Chen, Y. Lin, X. Liu, Z. Chen, C. Liu, H. Sun, X. Jin, Y. Yin and X. Li, *Nat. Commun.*, 2020, **11**, 1–9.
277 N. Siannas, C. Zacharaki, P. Tsipas, D. J. Kim, W. Hamouda, C. Istrate, L. Pintilie, M. Schmidbauer, C. Dubourdieu and A. Dimoulas, *Adv. Funct. Mater.*, 2024, **34**, 2311767.
278 Z. Cheng, H. Wang, Z. Guan, Z. Zhu, S. Shen, Y. Yin and X. Li, *ACS Appl. Mater. Interfaces*, 2025, **17**, 21440–21447.
279 Z. Guan, Z. Wang, S. Shen, Y. Yin and X. Li, *Adv. Mater. Technol.*, 2024, **9**, 2302238.
280 J. Y. Nau, *Rev. Med. Suisse Romande*, 2017, **13**, 878.
281 H. Sun, Z. Luo, C. Liu, C. Ma, Z. Wang, Y. Yin and X. Li, *J. Materiomics*, 2022, **8**, 144–149.
282 N. Zheng, J. Li, H. Sun, Y. Zang, P. Jiao, C. Shen, X. Jiang, Y. Xia, Y. Deng, D. Wu, X. Pan and Y. Nie, *Sci. Adv.*, 2025, **11**, 1–8.
283 J. Du, B. Sun, C. Yang, Z. Cao, G. Zhou, H. Wang and Y. Chen, *Mater. Today Phys.*, 2025, **50**, 101607.
284 S. Lee, G. An, G. Kim and S. Kim, *Appl. Surf. Sci.*, 2025, **689**, 162459.
285 S. Boyn, J. Grollier, G. Lecerf, B. Xu, N. Locatelli, S. Fusil, S. Girod, C. Carrétéro, K. Garcia, S. Xavier, J. Tomas, L. Bellaiche, M. Bibes, A. Barthélémy, S. Saïghi and V. Garcia, *Nat. Commun.*, 2017, **8**, 14736.
286 W. R. Ali and M. Prasad, *Sens. Actuators, A*, 2020, **301**, 111756.
287 B. Vigna, P. Ferrarini, F. F. Villa, E. Lasalandra and S. Zerbini, *Silicon Sensors and Actuators: The Feynman Roadmap*, 2022.
288 X. Da Xu, W. X. Zhang, X. H. Jia, Y. Z. Wu, H. Y. Kang, F. L. Chi and N. Gao, *Laryngoscope*, 2024, **134**, 937–944.
289 K. C. Balram and K. Srinivasan, *Adv. Quantum Technol.*, 2022, **5**, 2100095.
290 Y. Yansong, G. Liuqing and G. Songbin, *IEEE Trans. Microwave Theory Tech.*, 2022, **70**, 5185–5194.
291 T. Blésin, W. Kao, A. Siddharth, R. N. Wang, A. Attanasio, H. Tian, S. A. Bhave and T. J. Kippenberg, *Nat. Commun.*, 2024, **15**, 6096.
292 J. He and X. Sun, *Laser Photonics Rev.*, 2025, 2401525.
293 N. S. Yama, I.-T. Chen, S. Chakravarthi, B. Li, C. Pederson, B. E. Matthews, S. R. Spurgeon, D. E. Perea, M. G. Wirth, P. V. Sushko, M. Li and K.-M. C. Fu, *Adv. Mater.*, 2024, **36**, 2305434.
294 J. Zheng, X. Liu and Y. Yang, *IEEE Electron Device Lett.*, 2024, **45**(6), 1032–1035.
295 K. Alexander, J. P. George, B. Kuyken, J. Beeckman and D. Van Thourhout, *Conference on Lasers and Electro-Optics*, 2017, paper JTh5C.7.